Cent. Eur. J. Geosci. • 2(3) • 2010 • 270-305
DOI: 10.2478/v10085-010-0009-4

VERSITA

Central European Journal of **Geosciences**

The petrologic evolution and pre-eruptive conditions of the rhyolitic Kos Plateau Tuff (Aegean arc)

Research Article

Olivier Bachmann*

University of Washington,
Department of Earth and Space Sciences,
mailstop 351310, Seattle, WA 98195-1310

Received 9 March 2010; accepted 8 May 2010

Abstract: The Kos Plateau Tuff is a large (>60 km^3) and young (160 k.y.) calc-alkaline, high-SiO_2 rhyolitic ignimbrite from the active Kos-Nisyros volcanic center in the Aegean arc (Greece). Combined textural, petrological and geochemical information suggest that (1) the system evolved dominantly by crystal fractionation from (mostly unerupted) more mafic parents, (2) the magma chamber grew over $\geqslant$ 250 000 years at shallow depth (~1.5-2.5 kb) and was stored as a H_2O-rich crystalline mush close to its solidus (~670-750°C), (3) the eruption occurred after a reheating event triggered by the intrusion of hydrous mafic magma at the base of the rhyolitic mush. Rare banded pumices indicate that the mafic magma only mingled with a trivial portion of resident crystal-rich rhyolite; most of the mush was remobilized following partial melting of quartz and feldspars induced by advection of heat and volatiles from the underplated, hotter mafic influx.

Keywords: magmatic differentiation• crystal mush • rhyolite • silicic magmatism • Caldera-forming eruption • Aegean Arc

1. Introduction

Understanding the formation, storage conditions and eruption triggers of large silicic magma bodies is of obvious societal importance. These large accumulations of viscous, and volatile-rich magmas can lead to explosive eruptions of 100s to 1000s km^3 of material in a few days [1]. These events have devastating effects on a global scale, as their energy release are only matched by large asteroids impacts [2]. Despite being the ultimate hazard generated by our planet, the efforts put into unraveling what happens prior to and during these "supereruptions" remain inadequately limited (see [3]).

One such large, explosive eruption, referred to as the Kos Plateau Tuff (KPT; [4]) occurred ~160 000 years ago in the eastern Aegean region (Greece). The young age of deposits, and their excellent preservation in the dry Mediterranean climate provide an exceptional opportunity to dissect such a unit using the latest analytical techniques in petrology and geochemistry. This contribution reports detailed textural and geochemical information on all major phases (minerals and glass) that are present in this ignimbrite and provide insights into its evolution in the shallow crust and the processes that led to its eruption.

*E-mail: bachmano@u.washington.edu

2. Tectonic setting

2.1. Aegean Arc

The active South Aegean volcanic arc consists of volcanic centers (from W to E) of the Saronic Gulf (Crommyonia, Aegina and Methana) and the Aegean Sea (Milos, Santorini, and Kos-Nisyros). This magmatic activity is a result of northeastward-directed subduction of the African plate beneath the Aegean microplate (Figure 1) and erupted products display the typical calc-alkaline signature (e.g., [5]). The subduction zone is thought to have been active since the early Tertiary, and has been migrating south with time (with Oligo-Miocene magmatism in Thrace and Macedonia). This southward migration of the arc is most likely a consequence of roll-back of the subducted slab, but may also have been influenced by the westward motion of Anatolia (e.g., [6–9]). Convergence rate is around 1 cm/year [10], one of the slowest in the world [11].

The eastern sector of the arc, including the volcanic centers of Santorini and Kos-Nisyros is geodynamically very active and is at present a region of high tectonic unrest. Volcanic activity related to the modern Hellenic arc in the Kos-Nisyros area began at least 3.5 Ma ago [12]. Volcanism started with several andesitic, dacitic, and rhyolitic domes and pyroclastic flows of limited volumes, emplaced in different locations around the SW part of Kos island (Kefalos Peninsula; [13–15]). The largest volcanic deposit of the area (the Kos Plateau Tuff, hereafter KPT) erupted ~161 k.y. ago, generating > 60 km^3 of non-welded rhyolitic ash and pumice [4]. The KPT is best preserved on Kos, but is also exposed on the neighboring Greek islands of Tilos, Kalymnos, Pachia, as well as on the Turkish peninsula of Bodrum and Datça (see Figure 1; [16]). Isopach, isopleths and transport direction data indicate that the vent areas for the KPT were situated in the bay between southwest Kos and Nisyros volcano. The eruption is inferred to have formed a caldera at least 6-11 km in diameter, and perhaps as much as 20 km [16]. Subsequent activity, such as the Nisyros composite volcano (e.g., [17–24]), the Yali pumice cone and rhyolite lavas [25], the Pleistocene-recent Strongyle basaltic andesitic cone, and several submarine volcanoes in the area of Yali and Nisyros [26] all indicate that the Kos-Nisyros system remains magmatically active at present.

2.2. Analytical methods

Major elements were measured by X-ray fluorescence (XRF) on fused glass disks on a Phillips PW2400 spectrometer at the University of Lausanne (following the technique of [27]). The same samples were analyzed by XRF for trace elements using pressed-powder pellets. A small subset was chosen for analyses using inductively coupled plasma mass spectrometry (ICP-MS) at University of Lausanne. The analyses were performed using a 193nm Excimer laser and quadripole Perkin Elmer Sciex Elan 6100 DRC mass spectrometer on the glass disks. A deadtime of 90 seconds was counted before the ablation, which lasted about 20 seconds. The laser beam size was set to 120 µm with a power of 160 mJ. Helium was used as a carrier gas to transport ablated ions into the ICP-MS torch system.

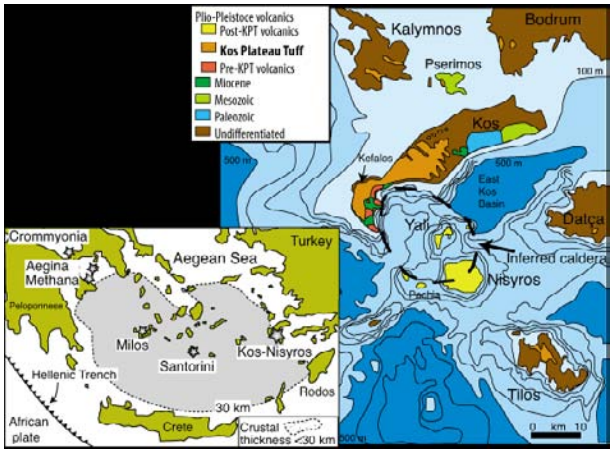

Figure 1. (a) Map of the eastern Mediterranean basin, showing the main active volcanic centers in Greece (modified from Bachmann et al., 2007). (b) Simplified geological map of the Kos-Nisyros Volcanic center.

All mineral phases were analyzed at University of Lausanne, using either the microprobes Cameca SX50 and Jeol 8600 Superprobe, except for quartz, that was analyzed at Rensselaer Polytechnic Institute (see [28] for operating conditions). Operating conditions in Lausanne were: accelerating voltage 15 kV, counting times 15-40 s on peak and 10 s on background, focused beam of about 1 micron for feldspars, Fe-Ti oxides, and amphibole, while defocused beam (5-20 microns) were used for biotites and glasses. Volatile elements (Na, Cl, F) were always analyzed first. Beam current was 10 nA for glasses and biotites, 15 nA for plagioclase, biotite and amphibole and 20 nA for Fe-Ti oxides. Standardization involved a set of natural and synthetic materials.

High Resolution Transmission Electron Microscopy (HR-TEM) analyses were performed at the University of Fribourg (Switzerland) using a Philips CM200 operated at 200 kV, equipped with an EDAX energy dispersive X-ray spectrometer (EDS). The beam diameter for the EDS analyses was 5 nm.

Sr and Nd isotopes on whole-rock samples were analyzed

at the University of Geneva, using a Finnigan MAT 262 system. The extraction process and analytical conditions followed those described in [29]). Oxygen isotopes were measured both at the University of Lausanne and University of Oregon. In Lausanne, minerals were laser-fused (using a CO_2 fluorination laser) associated with a Finnigan MAT 253 mass spectrometer. Standards used were NBS ($\delta^{18}O$ = 9.64‰) and LS ($\delta^{18}O$=18.1‰). The techniques at the University of Oregon are described in [30]).

2.3. Kos Plateau Tuff

2.3.1. Previous work

Notable previous work on KPT includes the petrological study of Keller (1969), who concluded that the KPT magma had been produced by partial remelting of a granitic body in the upper crust. Supporting evidence include: (1) the resorption of feldspar and quartz in KPT pumices, (2) the presence of glass-bearing granitic enclaves similar in whole-rock composition and mineralogy to the KPT magma, and (3) the highly evolved, near-eutectic composition of the matrix glass. Keller (1969) hypothesized that the reheating was a consequence of a new injection of more mafic magma beneath the cooling pluton, but no evidence of such a mafic magma was found at the time. Subsequent studies (e.g., [16, 31]) documented compositionally banded pumices, providing support for the hypothesis that the partial remelting event was indeed associated with the injection and limited mingling of more mafic magmas into the system.

Due to the importance of this unit as a geographically extensive stratigraphic marker (both on land and in submarine sediment cores), a detailed $^{40}Ar/^{39}Ar$ geochronological study was undertaken [32, 33]. Using the laser-fusion single-crystal technique on sanidine, the eruption age of the KPT has been precisely dated at 161.3 ± 1.1 k.y. [33]. In contrast, plagioclase revealed a more complex history, yielding four different ages populations at ~162 k.y. (indistinguishable from eruption age), ~271 k.y., ~925 k.y., and ~1728 k.y., indicating complex petrologic evolution involving crystal recycling [32].

The KPT eruptive stratigraphy was studied in detail by previous authors [16, 34–38]. The eruption began and ended with phreato-plinian activity (Units A, B and F of Allen, 2001). As the eruption rate increased, the style of activity changed to magmatic-volatile-driven, with the generation of relatively widespread, topographically-controlled ignimbrites (Unit D). Most of the volume was erupted during the climactic caldera-forming phase, which produced a widespread, highly energetic pyroclastic flow (Unit E, Figure 2). The change in fragmentation style from phreato-plinian to pre-climax and climax is recorded in the pumice clasts and ash shards.

Figure 2. Typical outcrops of KPT in the area of Kardamena (S central Kos Island), showing a ~15 m thick section of non-welded ignimbrite containing meter-sized andesitic lithics.

3. Magmatic components

The KPT is a non-welded pyroclastic deposit, consisting of juvenile ash (glass shards, crystal fragments), pumice as well as lithic fragments (some up to 3-4 m in diam; Figure 2) from different provenance (mainly andesite to dacite clasts, but also rare occurrences of schist, metabasalt, sandstone, limestone and rhyolite; [16, 32]). During the climactic part of the eruption (unit E), granitic clasts, some containing 10-20 vol% interstitial melt, were also erupted. These are *juvenile*, or co-magmatic clasts, as they have the same zircon age range as pumice samples do [39]. Several types of pumices can be distinguished on the basis of macroscopic characteristics [16]. Three petrologically useful categories can be isolated: (1) crystal-rich pumice (comprising both tube and frothy pumices), (2) crystal-poor pumices, and (3) banded (or grey) pumices. The texture, whole-rock composition, and mineralogy of each type of juvenile clasts are detailed below (see appendix 1 for pictures of thin sections and hand samples of all four pumices in the KPT).

3.1. Crystal-rich pumices

Crystal-rich pumices are by far the dominant juvenile clasts found in the KPT (>99%; Appendix 1.2 and 1.3). They vary in size from a few millimeters to almost a meter in diameter. The material is non-welded and a variety of textures has been described [16], although tube pumices are the most abundant pumice type (>90% of the pumice population; [40, 41]; see Appendix 1).

Crystal-rich pumices have crystal contents between ⩾ 25-35 vol% crystals [40]. The main mineral phases are, in decreasing order of abundance; plagioclase, quartz, sanidine, and biotite. Accessory phases included Fe-Ti oxides, apatite, zircon and monazite. Stadlbauer (1988) reports the presence of garnet, which has not been found in this study. Traces of barite ($BaSO_4$) have also been observed as inclusions in biotite (Figure 3).

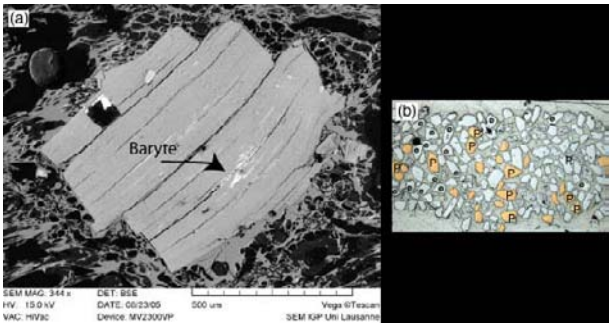

Figure 3. (a) SEM picture of a biotite from the Kos Plateau Tuff showing barite bands (see arrow). The glass around the crystal is fresh, suggesting that Baryte is not low-temperature alteration product. (b) Pyrite grains (P) in a heavy mineral separates from a KPT granitic enclave.

A striking characteristic of KPT plagioclase and quartz crystals is their frequently fractured and resorbed appearance (Figure 4, Appendix 1). Due to the high concentration of melt inclusions and melt channels in these two mineral phases, shattering most likely results from rapid decompression during magma ascent, leading to the exsolution of gas bubbles in the melt inclusions and explosion of the crystals (e.g., [42]).

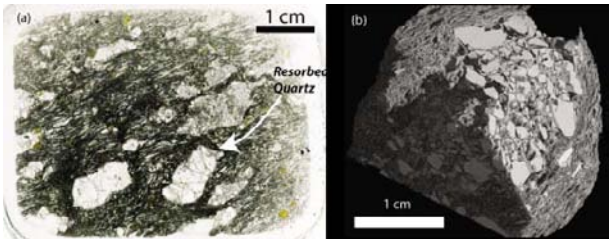

Figure 4. (a) Thin section photograph of a crystal-rich, tube pumice (pum2), showing small biotite phenocrysts, and large, partially shattered feldspar and quartz crystals with resorbed outlines (see similar images in Keller, 1969). (b) 3D reconstruction of a large KPT pumice (KPT06-34; See Degruyter et al., 2009) by X-ray tomography.

Well-preserved Rapakivi textures (plagioclase mantles over K-feldspar cores) have been observed in a few thin sections (Figure 5). However, most of the Rapakivi textures are found as sanidine fragments containing plagioclase inclusions and conspicuous Ba zoning (see the Mineral Chemistry section for more details on these textures).

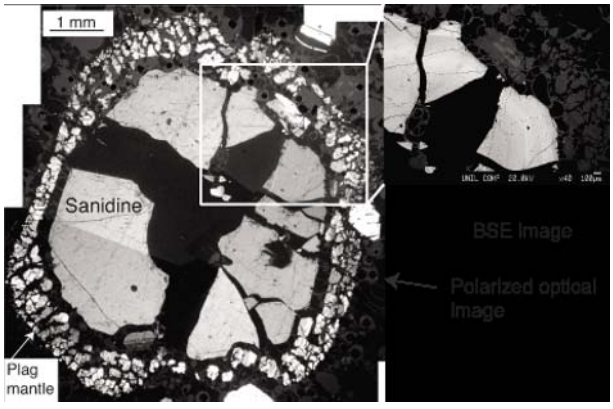

Figure 5. Blown-apart Rapakivi crystal found in a crystal-rich pumice (KPT05-42), showing a well-preserved plagioclase mantle. In the upper right corner, a SEM image shows Ba zoning in the sanidine.

3.2. Crystal-poor pumices

In early-erupted deposits (Units A and B), rare (< 1 vol%) crystal-poor pumices (<5-10 vol% crystals; [40]) can be found mixed together with the crystal-rich, tube pumices (Appendix 1). Crystal-poor pumices are generally small (few cm in diam.) highly porous (up to 80 vol% bubbles) and have dominantly small bubbles (microvesicular). Crystals are conspicuously smaller than in the crystal-rich pumices (<1 mm), and are generally fragmented. These pumices contain the same mineral assemblage as the crystal-rich type, including plagioclase, sanidine, quartz, magnetite, apatite, zircon and monazite (only ilmenite could not be found).

3.3. Grey and banded pumices

Grey and banded pumices can be found throughout the eruption sequence, although they are more conspicuous in Units D and E (Appendix 1). They remain nonetheless very rare (< 0.1 % of the total amount of pumice). They are generally 2-10 cm across, and have complex vesicle textures [43]. These pumices record the interaction between the resident rhyolitic magma and a more mafic end member, which contain rare and small crystals of hornblende and pyroxene [31, 40]. In most cases, mixing of the two magma types remained coarse (i.e., mingling), leading to conspicuous banding in the pumices. However, in rare cases, the mixing was more efficient, resulting in a pumice with a fairly homogeneous grey color.

3.4. Granitic enclaves

Granitic enclaves, similar to those described in rhyolitic units of the Taupo Volcanic Zone [44–46] can be found in the KPT (mostly in unit E; [4, 16]). These granitic enclaves are texturally variable (Figure 6); most contain glass at the boundaries between minerals (that has vesiculated, making samples very friable) but others are holocrystalline (no interstitial melt). The enclaves show a textural gradation from coarse-grained (with mm-sized crystals) to fine-grained, through intermediate bimodal textures (Figure 6a-c). Holocrystalline enclaves are typically finer-grained, suggesting more rapid cooling (Figure 6c).

When interstitial melt is present, it is mainly located at the grain boundaries, forming meandering channels (Figure 7). In some places, crystals faces are found against glass, suggesting late growth from a residual melt rather than partial melting (Figure 7e). Melt content measured in this study (by image analysis on BSE images) varies from 0 to ~20 vol%, but Keller (1969) claims that some granitic enclaves have melt up to 40-50 vol%.

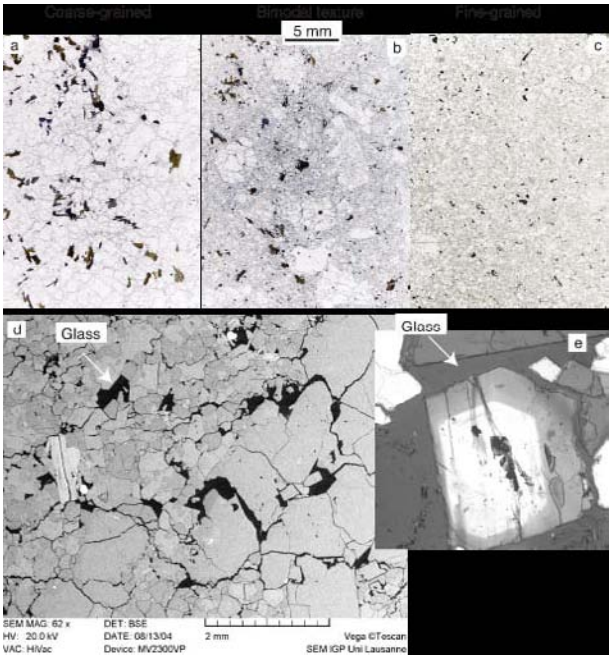

Figure 6. Granitic enclaves from the KPT (a) Xeno 2 (b) Xeno 4 (c) KPT04-15 showing different grain sizes: Xeno 2 is fairly coarse-grained, Xeno 4 has a bimodal texture, with coarse "phenocrysts" set in a finer matrix, and KPT04-15 is fine-grained. Image in (d) is a BSE photograph of Xeno 4, showing, in black, interstitial melt at the grain boundary (15% melt on this image) along with a few cracks. Crystal faces extending into melt zones (see arrows) suggest that melt is residual and not the result of partial melting.

The mineral assemblage of these granitic enclaves is identical to that of the pumice. In coarse-grained enclaves, plagioclase, biotite and some quartz crystals appear as large (mm-sized) and commonly fractured "phenocrysts", whereas the rest of the assemblage (Fe-Ti oxides, and anhedral quartz and K-feldspar crystals) fills the interstices. In addition to zircon, apatite and monazite, pyrite has been found in heavy mineral separates. As it is highly unlikely that these pyrite grains result from contamination during the separation process (no pyrite-bearing samples had been separated in the lab prior to these rocks), these pyrite crystals appear to be magmatic.

4. Whole-rock chemistry

Whole-rock compositions of the KPT determined for this study (see Appendix 2), are similar to previously published data [4, 16, 31] and typical for calc-alkaline rhyolites. The range in composition for all types of pumices (including grey-banded pumices) is from 71 to 76 wt% SiO_2, 3.5 to 5 wt% K_2O, and 0.2-1 wt% MgO (Figure 7). Trace element contents do not show particularly striking variations and/or trends, except Ba, which varies from 500 to 1100 ppm, Sr, with a range from 40 to 220 ppm and Rb with a range from 90 to 140 ppm (Figure 7 and 8, [31]). Note that crystal-poor, crystal-rich and granitic enclaves have overlapping ranges of both major and trace element composition, while interstitial glass in crystal-rich and banded pumices is slightly more evolved (lower Sr and higher Rb). The most evolved whole-rock samples are the holocrystalline enclaves, with compositions similar to KPT glass (Figure 7 and 8, [31]). Ratios, such as Ba/La and Ba/Ti, are also variable for this single eruption, with Ba/La ratios ranging from 12 to 45 in KPT juvenile clasts.

Whole-rock isotopic ratios of Sr, Nd and O ($\delta^{18}O$ of magma calculated from quartz data) for the KPT yield $^{87}Sr/^{86}Sr$ ~0.7035-0.7048, ε Nd +0.2 to +1, and $\delta^{18}O$ of ~8 ± 0.5 ([39]; Figure 9 and 10, Table 1). The Sr-Nd range in the KPT (and Kos-Nisyros complex; [23, 24, 47]) is similar to (albeit less extensive than) the Santorini data [48, 49]. Volcanic rocks in Milos and centers of the Saronic gulf (Aegina, Methana, and in particular Crommyonia) generally have more radiogenic Sr and less radiogenic Nd isotopic ratios [48, 50] than Santorini and Kos-Nisyros. Interestingly, the magmas with highest $^{87}Sr/^{86}Sr$ and lowest ε Nd in both Milos and Nisyros are the more mafic ones (andesites; [23, 24, 48]). The wide (and poorly-defined) range of $^{87}Sr/^{86}Sr$ and ε Nd values obtained from samples of Nile sediments are indicated for reference (e.g., [51, 52]).

Figure 7. Selected whole-rock major element diagrams showing the compositional variability in the KPT juvenile enclaves. Ranges are similar to those reported by Stadlbauer (1988). The interstitial glass composition of several KPT pumices (electron microprobe analysis) is also provided.

5. Phase chemistry

5.1. Glass

Major and trace element composition of both matrix glass and melt inclusions were analyzed in the KPT by microbeam techniques (electron microprobe and LA-ICPMS) and were published in previous papers [53, 54]. This glass is similar in both populations and typical for a high-SiO_2 rhyolite. All Major and most trace elements show a low variability [54]. Only Ba and Sr display significant (and positively correlated) variations (Sr from 10 to 60 ppm, Ba from 200 to 1000 ppm), indicating an effect of feldspar fractionation. REE elements are typically low in abundance, with a bowl-shape pattern (depletion in MREE), and have small Eu negative anomalies [53].

5.2. Feldspars

K-feldspars (sanidine in the volcanic rocks, and orthoclase in the granitic enclaves) vary from Or60 to Or80. The most K-rich feldspars are found in the holocrystalline enclaves, while the most K-poor (due to Ba content up to 4.5 wt% BaO, 8 mol% Celsian) are present in melt-bearing granitic enclaves. K-feldspars from banded, crystal-poor and crystal-rich pumices have a similar range of Or values (average ~Or67). Apart from zoning in Ba, KPT K-feldpars do not show any major chemical heterogeneities (e.g., Figure 11 and 12).

As for K-feldspars, plagioclase crystals show a similar range of compositions for all juvenile clasts in the KPT (An45-An10) with the most evolved (lowest An content) in the holocrystalline granitic enclave (Figure 13, 14, 15). The most Ca-rich zones (>An40) are found uniquely in cores (even in banded pumices), and suggest inheritance from a more mafic stage of differentiation. These cores are, however, rare, and the dominant volume of the plagioclase in the KPT oscillate between ~An17 and An25.

Most KPT plagioclase crystals have oscillatory zoning patterns superimposed on a progressive increase in An content towards the rim (from ~An17 and An25, see examples on Figure 13 and 14). This pattern is even observed in granitic enclaves, if the outmost rims, reflecting very late growth, is removed; Figure 15). As closed-system crystallization would induce a decrease in An towards the rim ("normal" zoning), this progressive inverse zoning requires an explanation. Considering that the system was

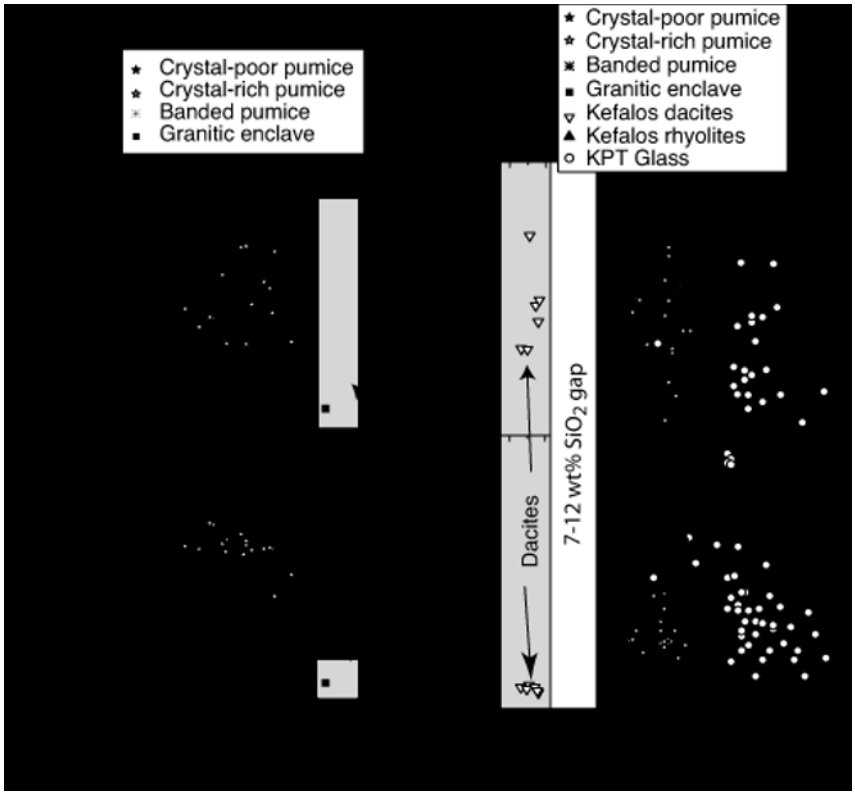

Figure 8. Selected trace element concentrations and ratios as a function of SiO_2 and Rb in pumices, granitoïd enclaves and melt inclusions-matrix glass of the KPT. Sanidine-free Kefalos dacites and rhyolites are also shown for comparison.

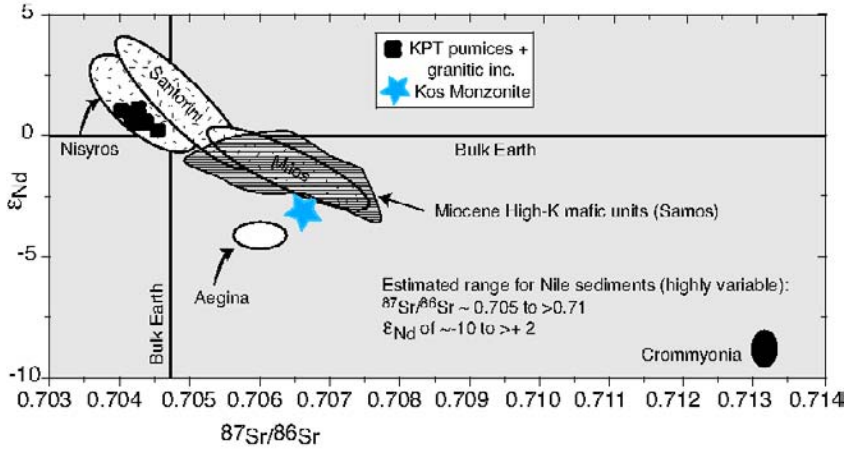

Figure 9. Sr-Nd isotopic ratios for whole-rock KPT samples (Unit B to E, including granitic enclaves) plotted with data from other quaternary volcanic deposits in the Aegean Arc (Data from [23, 24, 48–52, 88, 89, 117, 118]).

crystallizing over a limited pressure range (upper crust), An content could increase due to (1) changes in the melt chemistry (increase Ca content), (2) increase in H_2O in the magma, and (3) increase in temperature (e.g., [55, 56]). If Ca was increasing in the melt, we would expect other elements, such as Fe and Sr to increase concurrently. As Fe and Sr content do not vary significantly across inversely zoned plagioclase crystals (Figure 14), a change in magma

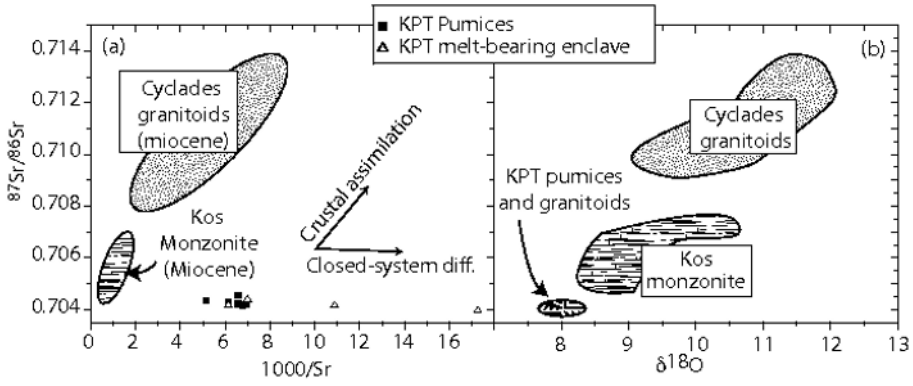

Figure 10. (a) Whole-rock Sr isotopic ratios as a function of 1/Sr and (b) for Sr-O isotopic ratios for KPT samples, data is compared to local monzonite and Cyclades granitic intrusions (data from [87, 118]).

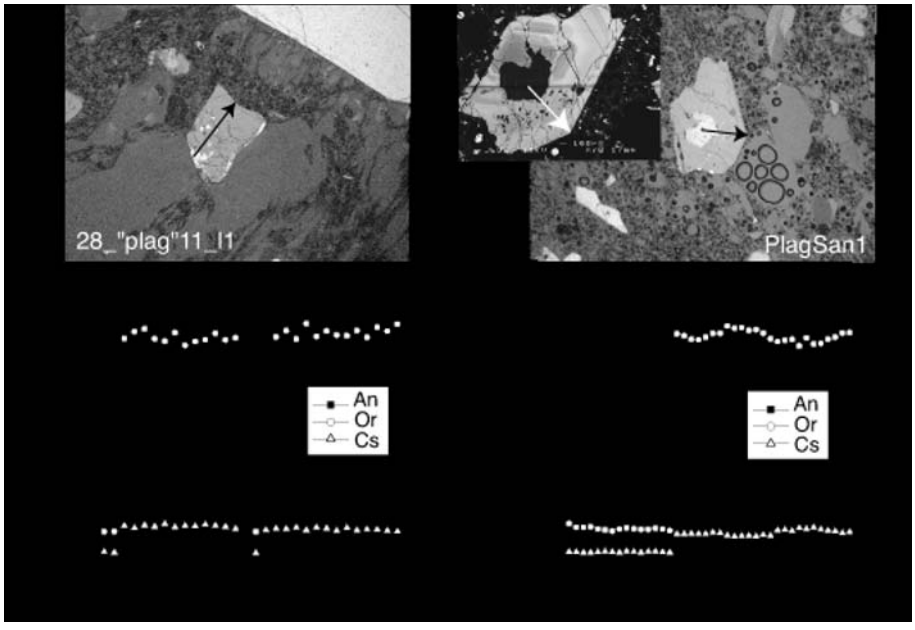

Figure 11. Sanidine crystals with plagioclase inclusions in optical continuity in a crystal-rich pumice (KPT04-28), and zoned in Ba (SEM image in upper right corner). They represent fragments of Rapakivi crystals.

temperature and/or an increase in H_2O is a more likely scenario.

The most striking textural and geochemical feature of feldspars in the KPT is the large Rapakivi grains (K-feldspars mantled by plagioclase, [57], Figure 5), and the ubiquitous sanidine crystals with plagioclase inclusions (fragments of Rapakivi crystals, Figure 11). Associated with Rapakivi textures is obvious Ba zoning (Figure 16), which reflects different generations of sanidine growth during Rapakivi formation due to the following process. As sanidine resorbs during heating, it releases Ba into the melt, which the co-precipitating plagioclase does not incorporate. Therefore, as temperature drops, the new generation of sanidine will crystallize from a Ba-rich melt, inducing the observed zoning patterns, with high Ba immediately inboard of the resorption surface. Ba zoning has been reproduced experimentally by temperature fluctuations in a chemically closed-system [58]. These Ba zoning patterns recording temperature fluctuation in magmas have been observed in other volcanic systems [59, 60], and are in agreement with the inverse zoning patterns in plagioclase.

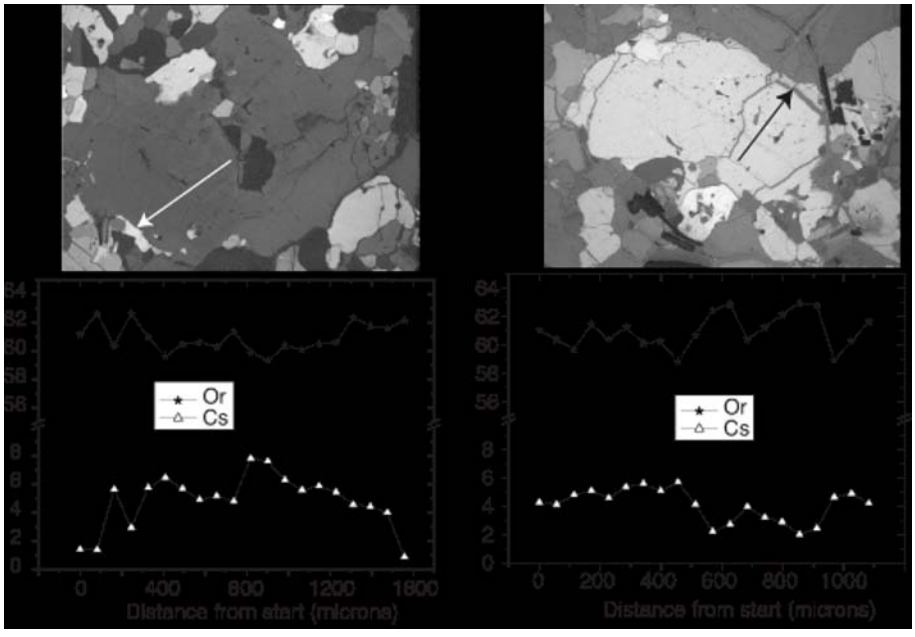

Figure 12. Electron microprobe profiles in K-feldspar crystals of a representative melt-bearing granitic enclave (KPT04-20).

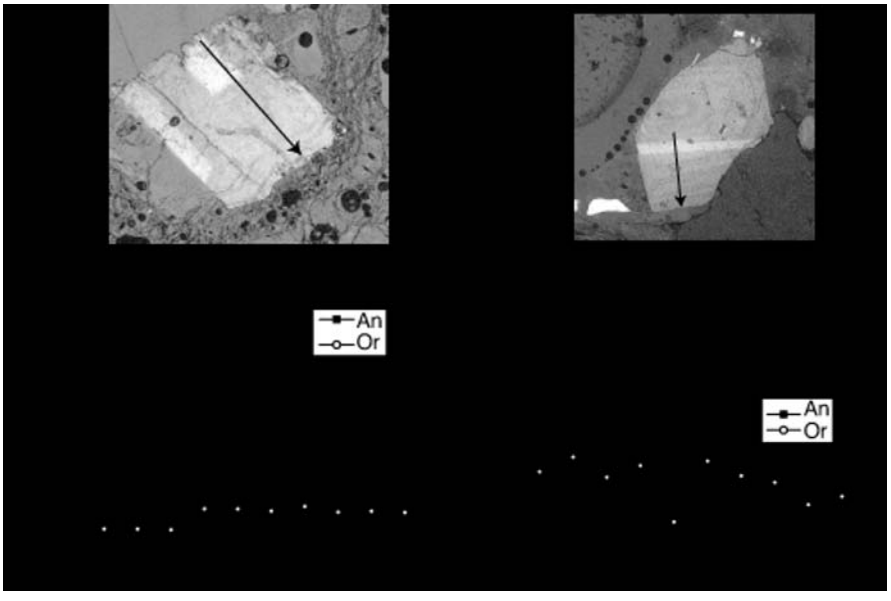

Figure 13. Reverse zoning (An increase towards the rim) in plagioclase crystals of the Kos Plateau Tuff (from tube pumice samples collected at different stratigraphic levels of the unit). Note also the An-rich cores, suggesting growth from a more mafic magma).

5.3. Biotite

Biotite crystals in the KPT form 1-5 modal% of the mineral assemblage. Crystals are generally euhedral but show bands of different shades of brown (from dark brown to yellowish-brown under natural light) and extreme fragility under the electron beam (Appendix 3). In addition, approximately 90% of the electron probe analyses in all samples (pumices and granitic enclaves) yield low sums of total oxides (sums between 80-95%; Figure 17) despite reasonable analytical conditions (mostly done at 15 kV and 15 nA at the University of Lausanne, see earlier section and [60]

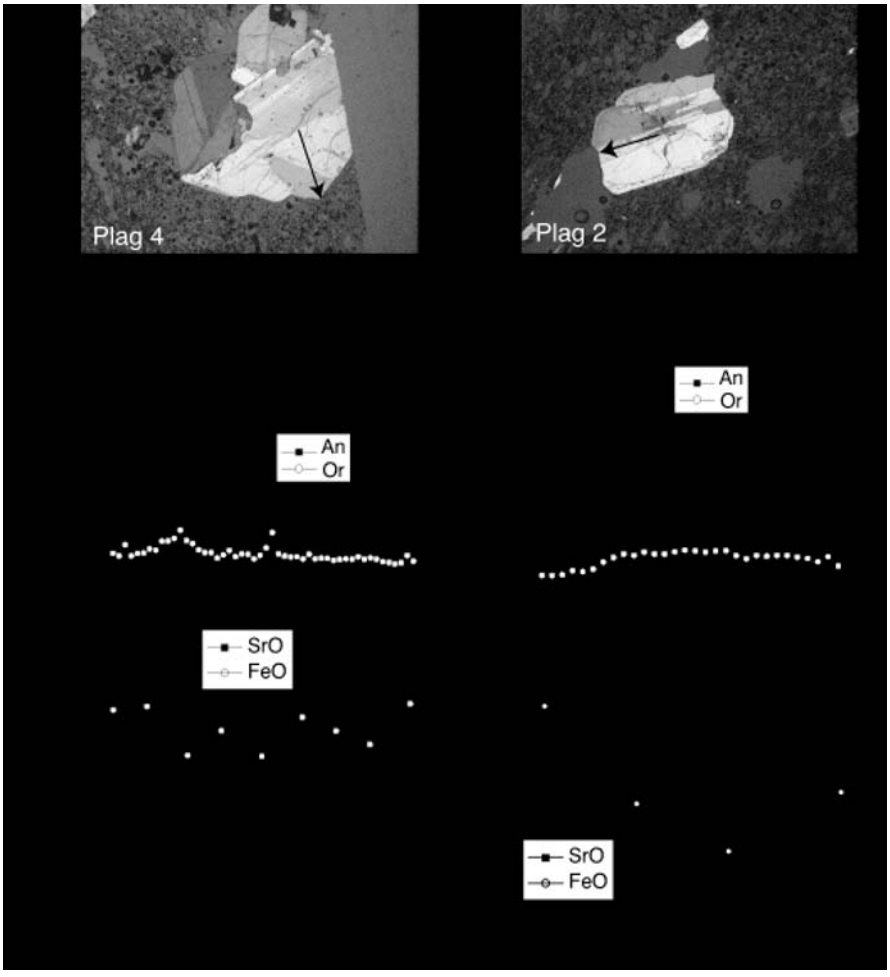

Figure 14. Electron microprobe traverses in plagioclase from two crystal-rich KPT pumice (KPT04-28 and KPT04-3), showing complex An variation (including a noticeable increase in An at the rim) while Sr and Fe contents remain nearly constant.

for analytical details), careful and complete calibration of all important elements (SiO_2, TiO_2, Al_2O_3, FeO, MnO, MgO, CaO, BaO, Na_2O, K_2O, F, Cl), defocused beam (up to 20 microns in diameter) and good sums of total oxides in biotite standards. Sharp drops in some elements, which could indicate interlayering with other phases (such as drop of K in interlayered chlorite) is not observed (Figure 17), and LA-ICP-MS trace element data are compatible with pure biotite (See Table 2 and for analytical conditions and results). Only Na_2O increases (from 0.5 to >3 wt%) from biotites with normal sums (96± 1 wt%) to biotites with low sums (Figure 17).

High Resolution Transmission Electron Microscopy (HR-TEM) observations on KPT biotite crystals do not show any sub-micron interlayering with other phases. XRD spectra on the (001) plane can be interpreted as biotite crystals of different sizes (Appendix 4). TEM-EDS analyses down to the nanometer scale yield annite-rich Ti-biotite compositions with some unusual components. All spectra show a Cl peak with variable intensity (Figure 18). In addition to K, two other potential interlayer cations show up in the spectra, Na and Ca, and there is a correlation between the size of the Ca, Na and Cl peaks. Chlorine can be incorporated in biotites, but amounts larger than 0.2 wt% are rare, with maximum amount around 2.5 wt% [61]. Similarly, Na and Ca are rarely above 1 wt% [62]. This suggests the presence of a Cl, Na and Ca-rich, sub-micron sized separate phase (halite or NaCl crystals or brines; [61, 63]).

Biotites with low analytical totals and chemical evidence for the introduction of mobile elements also occur in the basal, highly evolved Bishop Tuff [64]. In both the Bishop Tuff and KPT case, the freshness of all other phases (including glass), the absence of vapor phases effects, and

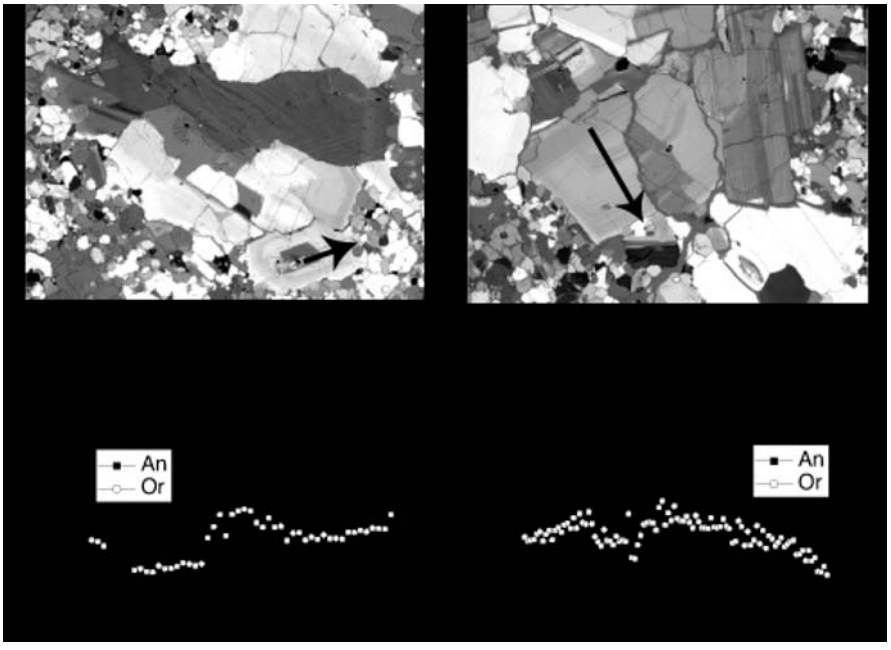

Figure 15. Electron microprobe traverses in plagioclase from two large plagioclase â€phenocrystsâ€{ from a melt-bearing granitic enclave (Xeno4), showing similar flat to increasing An content toward the rim.

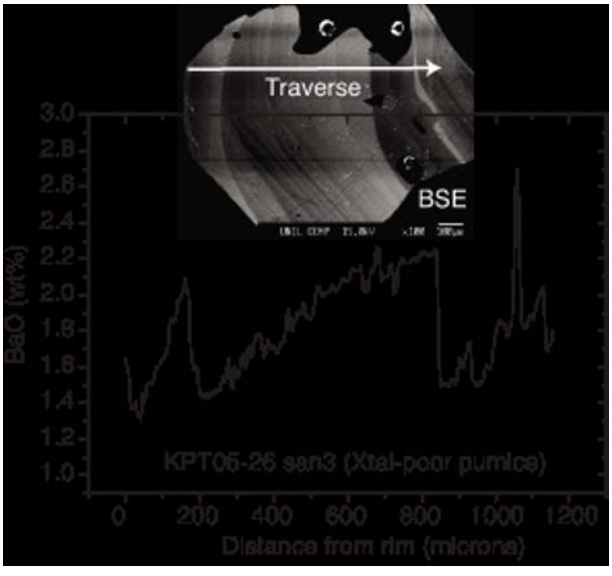

Figure 16. Ba zoning in a sanidine crystal from a crystal-poor KPT pumice (obtained by applying grey-scale calibration on the BSE image using the Scion Image Software).

the abrupt quenching due to explosive eruption and non-welded deposits argue against a post-eruptive interaction with hot water. As suggested by Hildreth (1977), the preferred interpretation is that biotite trapped many fluid inclusions in the volatile-enriched magma chamber, probably in response to the presence of an exsolved brine phase.

In the few biotite electron microprobe analyses with reasonable totals (between 95-97 wt% total oxides) that have been collected, major element compositions are fairly similar throughout the eruptive sequence (Figure 19), except for elements that are highly sensitive to temperature, such as Ti and F [65]. Low Ti and high F contents in biotite crystals from holocrystalline granitic enclaves are compatible with the low temperature of these samples, while the high Ti and lower F in crystal-rich and crystal-poor pumices is consistent with higher temperature around 670-750°C (see Fe-Ti oxides section below).

5.4. Fe-Ti oxides

Both ilmenite and magnetite microphenocrysts are present in most KPT samples, including melt-bearing and holocrystalline granitic enclaves. However, ilmenite is generally in low abundance, and none have been found in the crystal-poor pumices. When present, both phases are generally homogeneous and in equilibrium with respect to Mg/Mn contents (except for some granitic enclaves; method of [66]. Ilmenites found in melt-bearing and holocrystalline granitic enclaves have very high Mn content (between 5-6 wt% MnO for the melt-bearing gran-

Table 1. Oxygen isotopic ratios of quartz, Magnetite and biotite of a crystal-rich, tube pumice of the KPT (KPT-04-21).

	Mineral phase	Number of analyses	$d^{18}O$‰	Qz-Mt T, °C [81]
		University of Lausanne		
KPT04-21	Quartz	3	8.79	754±10°C
KPT04-21	Magnetite	3	2.79	
		University of Oregon		
KPT04-21	Quartz	2	8.53	
KPT04-21	Magnetite	2	2.63	762±10°C
KPT04-21	Biotite	3	6.61	
KPT04-21	melt		~ 8 ± 0.5	Assuming a 0.5‰difference between melt and Quartz at 760°C [120]

Oxygen isotope ratios for quartz, biotite and magnetite (between 1.3 and 2.8 mg) were determined at the University of Lausanne and University of Oregon (Table 1, main text) using a CO_2 laser to fuse crystals. At Lausanne, standards NBS (at $d^{18}O$ of 9.64‰, and LS ($d^{18}O$ of 18.1‰) were used at the beginning and the end of each sequences of analyses. Using quartz $d^{18}O$ values (~8.5± 0.5‰), the KPT melt $d^{18}O$ value (~8± 0.5‰) was determined by subtracting ~0.5‰of the quartz ratio, which is considered to be the melt-quartz fractionation at ~760°C [120].

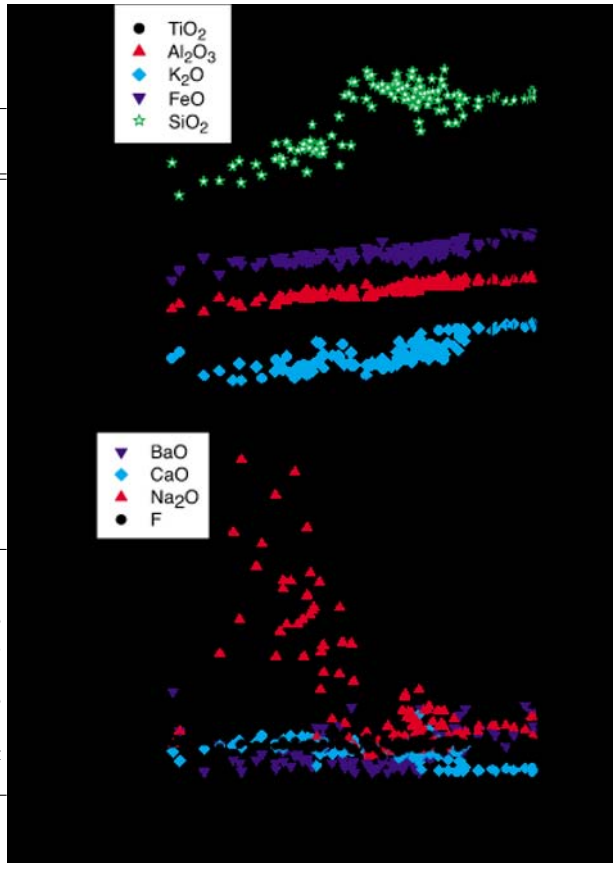

Figure 17. Electron microprobe analyses of biotite crystals from the Kos Plateau Tuff. Only a small fraction of the analyses give totals of wt% oxide that are satisfying (between 95-97 wt% oxide for biotite, assuming 4±1 wt% water). Low totals appear to be due to a diluting agent; all major oxides show abundances that progressively decrease, as totals get lower. All analyses done at the University of Lausanne with typical analytical conditions for these minerals (see text and Bachmann et al., 2002 for details).

itoids, and 7-13 wt% MnO for the holocrystalline ones).

5.5. Quartz

Quartz appears as large irregular crystal fragments in most cases. They contain numerous melt inclusions, and the largest of which (>200 microns) decrepitated upon eruption, blowing the crystals apart. This quartz fragmentation has been described in many other deposits from explosive volcanic eruptions [42, 67]. In addition to decrepitation, Keller (1969) reported that all light colored crystal phases in the KPT (including quartz) show strong corrosion, resorption, and melting. Although plagioclase crystals do appear euhedral in some cases, this study confirms that most quartz and sanidine crystals show irregular, resorbed outlines (part of it resulting from decrepitation of grains).

Cathodoluminescence (CL) imaging of these quartz crystals reveal limited and smooth zoning. As CL zoning in quartz is thought to be related to Ti content [68], which correlates with temperature [69], electron and ion microprobe analyses have been performed in order to determine the Ti contents of these quartz crystals (see [28] for analytical details). As suggested by CL images, Ti gently (± some oscillatory zoning) decreases towards the rim (Figure 20 and Appendix 5). In contrast to quartz crystals in the Bishop Tuff [28, 70], no bright Ti-rich rims, which have crystallized at higher temperature, have been found. As other evidence for late reheating are present in the Kos Plateau Tuff magma (Rapakivi textures and inverse zoning in plagioclase), a possible explanation would be that quartz did not grow during the reheating event. This interpretation is consistent with the generally rounded external shapes of quartz crystals, which indicate late resoption (see also [4]).

5.6. Amphibole

Amphibole crystals in the KPT are only found as rare and small crystals in banded pumices, and are associated with the mafic magma mixed or mingled with the ambient

Table 2. KPT Biotite analysis by LA-ICP-MS.

	KPT Pum3 (Frothy)			KPT Pum2 (tube)			Bfc 113 (FCT-O)			KPT/FCT
	Av. (N=11)	SD	Rel. SD	Av. (N=9)	SD	Rel. SD	Av. (N=6)	SD	Rel. SD	
Li	195	52	26%	68	20	30%	75	13	18%	0.9
P	n.m.	n.m.	n.m.	n.m.	n.m.	n.m.	20	22	113%	-
S	n.m.	n.m.	n.m.	n.m.	n.m.	n.m.	21	4	19%	-
Sc	23.2	1.2	5%	23.9	1.2	5%	9.9	0.7	7%	2.4
Cr	14	5	38%	16	3	18%	8	3	34%	2.1
Ni	250	126	50%	25	11	44%	31	1	5%	0.8
Rb	250	42	17%	294	85	29%	469	13	3%	0.6
Sr	29	4	14%	18	6	35%	8.7	1.2	14%	2.0
Y	3.23	1.06	33%	3.14	1.60	51%	0.08	0.04	46%	39
Zr	2.1	0.6	29%	2.1	0.3	16%	3.4	0.4	11%	0.6
Nb	59.9	6.2	10%	62.7	1.5	2%	46.7	0.5	1%	1.3
Cs	2.2	1.0	47%	3.0	1.2	39%	3.1	0.3	8%	1.0
Ba	965	502	52%	1561	933	60%	1613	291	18%	1.0
La	2.12	3.21	151%	2.49	1.63	66%	0.02	0.02	114%	124
Ce	2.94	4.16	142%	3.96	4.29	108%	0.13	0.19	141%	30
Nd	1.47	1.21	82%	2.31	1.80	78%	<0.01	-	-	-
Sm	0.32	0.11	36%	0.51	0.40	77%	<0.01	-	-	-
Eu	0.08	0.03	38%	0.07	0.04	54%	0.1	0.02	23%	0.7
Gd	0.48	0.21	44%	0.42	0.30	71%	0.05	0.07	136%	8.3
Dy	0.38	0.13	36%	0.42	0.25	60%	0.03	0.03	100%	14
Er	0.26	0.11	42%	0.27	0.16	61%	<0.01	-	-	-
Yb	0.31	0.16	51%	0.27	0.14	51%	0.02	0.03	221%	14
Hf	0.08	0.05	67%	0.10	0.06	63%	0.42	0.13	32%	0.2
Ta	1.2	0.1	9%	1.2	0.1	8%	1.17	0.06	5%	1.0
Pb	12.20	8.36	69%	10.52	8.86	84%	1.87	0.19	10%	5.6
Th	0.32	0.76	238%	0.09	0.06	66%	0.02	0.03	138%	4.7
U	0.1	0.1	101%	0.1	0.1	56%	0.11	0.09	79%	1.1

LA-ICP-MS analyses were done on both fused disks used for XRF analysis and on some of thin sections used for the microprobe analyses. The analyses were performed using an Inductively Coupled Plasma torch associated to a quadrupole Perkin Elmer Sciex Elan 6100 DRC mass spectrometry of the University of Lausanne. A deadtime of 90 seconds was counted before the ablation, which lasted about 20 seconds. The laser beam size was set to 120 µm with a power of 160 mJ on the glass disks and 40 µm on thin sections. Helium was used as a carrier gas to transport ablated ions into the ICP-MS torch system. The spectrometer was optimized on low background values, to take in account low content in trace elements. The standards NIST 612 (CaO = 11.93 wt%) and NIST 610 (CaO = 11.827 wt%) were used respectively, at the beginning and at the end of each analytical sequence with results always within ± 10% of the reported values by NIST. Precise wt% Al_2O_3 from microprobe values were used as internal standards. Data reduction done with LAMTRACE, a spreadsheet developed by S.E. Jackson (Macquarie University). N = Number of different crystals analysed. Analytical SD is typically 1-5% of the measurement, and typically much smaller than reported geological SD.

rhyolite. They form mm-sized euhedral crystals with no apparent chemical zoning. Only a few electron microprobe analyses were collected at the University of Lausanne (see analytical methods). These amphiboles can be classified as magnesiohornblendes (using [71]).

6. P-T-F_{O2} conditions of the KPT

As shown by Keller (1969), the normative composition of the KPT glass falls near the water-saturated haplogranitic eutectic at 2 kb (accounting for the effect of Ca; Figure 21). It provides an estimate of the pressure at which the glass last equilibrated with the mineral assemblage. This shallow pressure of equilibration is agreement with the range

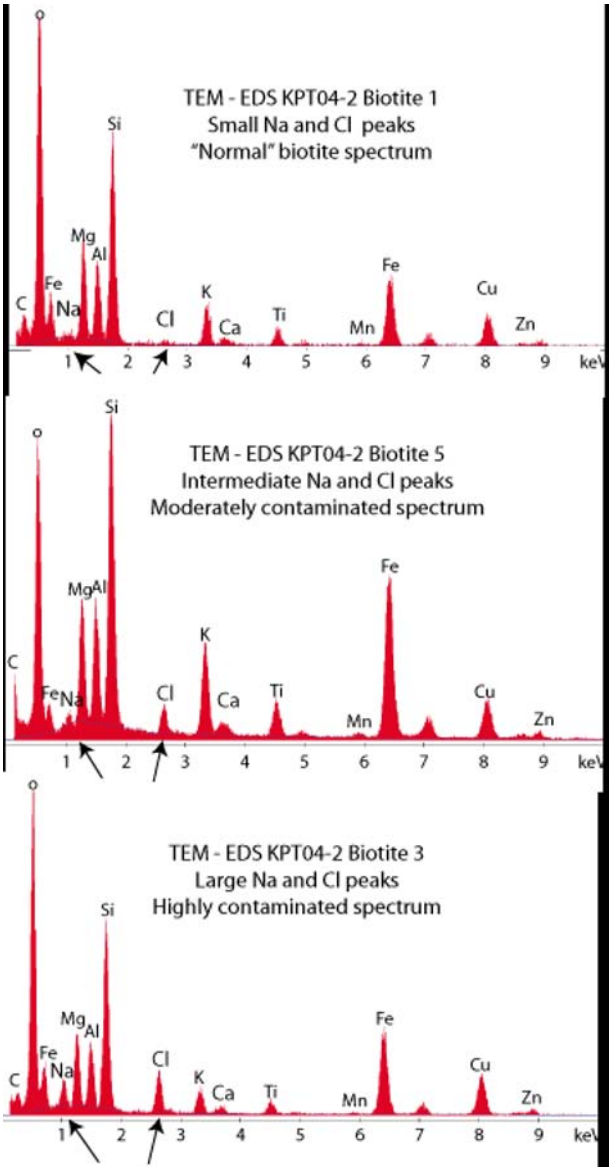

Figure 18. TEM-EDS spectra of KPT biotites, showing abnormally high Cl, Na, and Ca is the structure, suggesting the presence of a Na, Cl, and Ca rich sub-micron phase within the biotite.

of volatile saturation pressure obtained by CO_2-HO_2 content of quartz-hosted melt inclusions (1.5-2.5 kb; [54]). In any case, such a high-SiO_2 magma must have been produced at shallow depth, as pressures higher than 2-3 kilobars increase the stability field of quartz, and lead to a lower SiO_2 content in the residual liquid (e.g., [56]).

Oxygen fugacity for the KPT rhyolite is high (NNO +0.5 to 2, using respectively the calibration of [72] and [73]; Figure 22), but not unusual for arc magmas (e.g., [72, 74]). Such highly oxidized magmas are commonly associated with high magmatic S content (although little remains dissolved in the melt at low temperature; [75]), and the presence of sulfate in the deposits (e.g., [76–78]).

Magmatic temperatures of the different sample types in the Kos system have been estimated by six different thermometers, including as Fe-Ti oxides pairs (see next paragraph), two-feldspars pairs [79], amphibole-plagioclase pairs [80], quartz-magnetite δO^{18} partitioning [81], Ti-in-Quartz [69], and zircon saturation temperature [82].

Many calibrations of the Fe-Ti oxides thermometry have been published over the years (see the most recent one, [72], for a comparison of the different versions). In the case of the KPT, the difference between temperature using the Ilmat spreadsheet [83] with the calibration of [73] and the Ghiorso and Evans (2008; [72]) calibration yield about 100°C difference for the same sample Fe-Ti oxides from pumice samples yield ~770°C for the calibration [73], and ~670°C using [72]. Although it includes the most up-to-date database of experiments, and should be particularly appropriate for arc magmas, the calibration of [72] appear to yield very (too?) low temperatures. In this particular case of the KPT, it yields pumice Fe-Ti temperatures similar to or below the solidus for a haplogranite composition at P_{H_2O} = 2 kb [84], while melt-bearing granitic enclaves are much lower than the solidus.

In addition to the Fe-Ti oxides thermometer, magmatic temperature for the KPT pumices obtained using (1) two-feldspar equilibrium, (2) Quartz-Magnetite δO^{18} partitioning, (3) Ti-in-Quartz [69], and (4) Zircon saturation, all fall within 50-80°C of the water-saturated haplogranite solidus. The lowest temperatures are given by two-feldspar thermometry (average of the different thermodynamic models are ~700°C; Figure 23), Ti-in-Quartz thermometry yields 700-750°C (at an aTi = 0.9; [69, 85], Appendix 5), and Qtz-Mag δO^{18} thermometry clusters around 750-760°C [81]. Zircon saturation temperatures [82] cluster around 730°C (Figure 24).

7. Discussion

7.1. Rhyolite differentiation process in the Aegean

There seem to be little doubt that fractional crystallization (FC) is the dominant differentiation mechanism for the KPT, and more generally within the whole Kos-Nisyros volcanic center; most petrological studies that have focused on magmas in the area indicate a very limited amount of assimilation of crustal wall rocks in Kos-Nisyros magmas [17, 19, 24, 39, 48, 86]. This is confirmed by new Sr-Nd-O isotope data on multiple samples of the KPT ob-

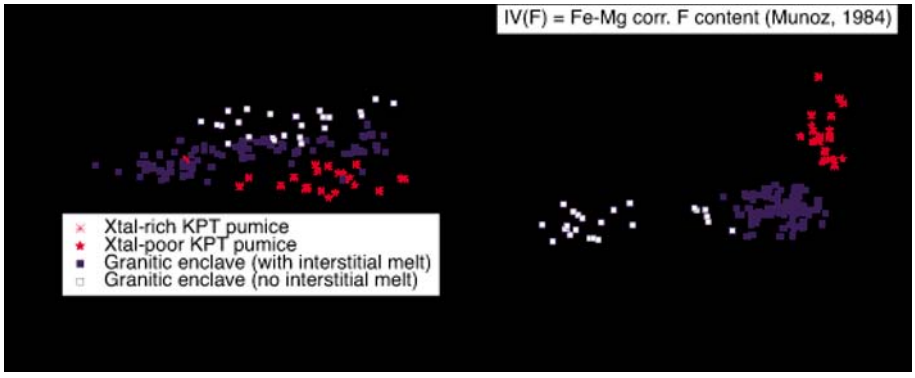

Figure 19. Electron microprobe analyses with satisfying totals (analytical totals between 95 and 97 wt%) of KPT biotite in pumices and granitic enclaves. Despite a fairly wide range in SiO_2 content, major elements vary little except those which are related to T (particularly F and Ti, [65]). IV(F) yields a F value corrected for Fe/Mg variation [65].

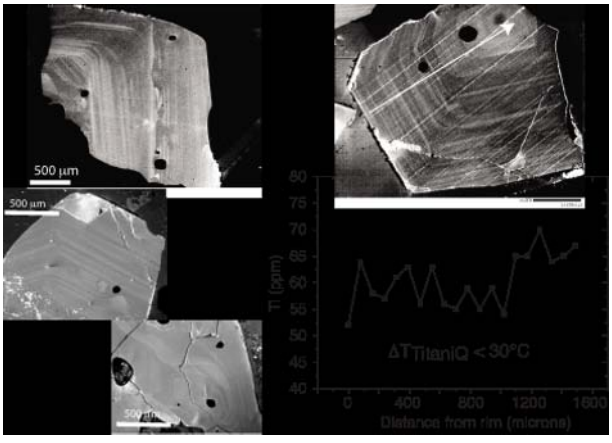

Figure 20. Cathodoluminescence image and traverse across a quartz crystal from the KPT (KPT21-2), showing a normal zonation in Ti (decrease concentration = decreasing temperature) towards the rim. The temperature variation based on the TiTaniQ calibration [69] gives a range of temperature from core to rim of ~30°C)

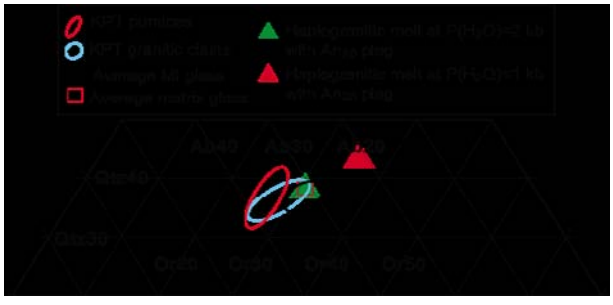

Figure 21. Haplogranite ternary with the plotted normative composition of the KPT interstitial melt. The norm of crystal-rich pumices, banded pumices and granitic enclaves are also plotted for reference; they show a higher An content due to the presence of plagioclase crystals.

tained in the course of this study, which imply that extensive participation of the old Paleozoic-Mesozoic basement or Miocene plutons (e.g., [87]) found in the area could not have been a major component in forming the local dacites and rhyolites. In addition, the absence of xenocrystic material in more than 150 ion probe data points in KPT zircons imply that wall rocks did not contribute much to the mass of zircons (and mass of magma by inference).

While fractional crystallization is likely to be the main process that drives differentiation in the Aegean, it is certain that some crustal material, either under the form of subducted sediments from the Nile delta, old crustal material hosted in the mantle or from Paleozoic-Mesozoic continental rocks from the overriding Aegean plate, has participated in a limited extent in the generation of the KPT. On the basis of the fact that isotopic tracers show as much or more crust in the more mafic magmas (andesites) than dacites and rhyolites in Kos-Nisyros volcanic center (true also elsewhere in the Aegean; [24, 48]), it is likely that the assimilation has occurred deep (either in the lower crust or the upper mantle). However, precisely determining the relative contributions from the different reservoirs (slab, subducted sediments, asthenospheric mantle, metasomatized lithospheric mantle, overriding continental plate) in the Aegean using Sr and Nd isotopes is unachievable in the present state of knowledge. It is not surprising that the continental crust from the Aegean microplate is isotopically highly variable (e.g., $^{87}Sr/^{86}Sr$ from ~0.704 to ≫0.71; see among many [87–89]), but it is also known that European lithospheric mantle can be highly heterogeneous ($^{87}Sr/^{86}Sr$ >0.715; [90–93]; see also discussion in [94] and a trachyandesite clast found in the KPT, [47]), while Nile sediments show a large range

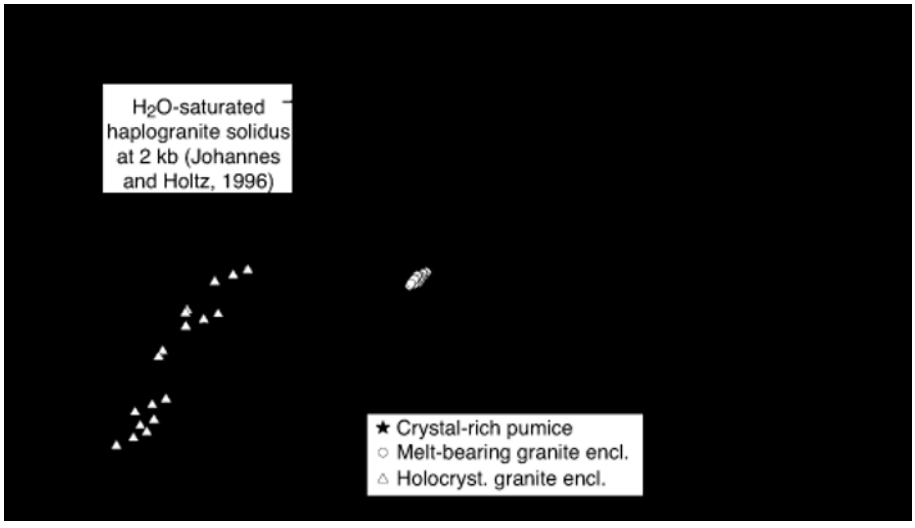

Figure 22. T-fO_2 diagram using Fe-Ti oxides (using Ilmat spreadsheet of Lepage (2003) and the calibration of Andersen and Lindsley, 1985, [73]) present in samples of the KPT superimposed on thermodynamic data for S (compiled from [119]). Granitic clasts contain pyrite in heavy minerals separates, in agreement with thermodynamic data. Temperatures given by QUILF95 and [72] calibrations are shown for comparison.

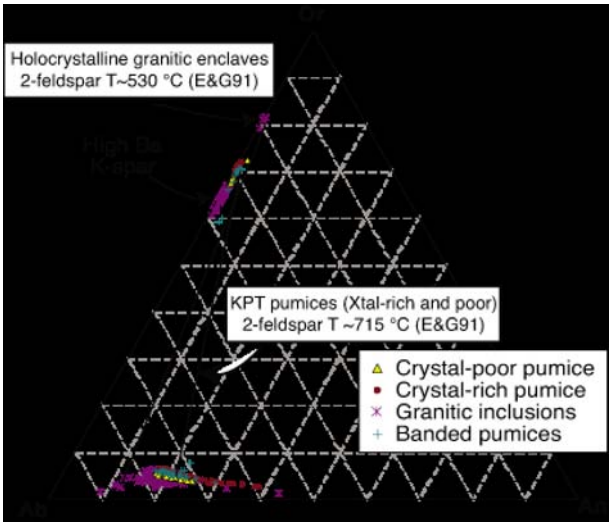

Figure 23. Feldspar ternary diagram showing the compositional ranges of KPT feldspars. 2-feldspar Temperature using SolvCalc [79] are also displayed.

Figure 24. Summary of temperature data obtained on KPT samples. G&E08 is Ghiorso and Evans, 2008 [72], and A&L85 is Andersen and Lindsley, 1985 [73].

of isotopic values as well (see Figure 9; [47]; [51, 52]). In these conditions, mixing calculations, which require well-defined endmembers, leave significant uncertainty in the determination of the relative proportion of each endmembers in the final rhyolitic magma.

Similarly, the $\delta^{18}O$ ratio indicates a major mantle component in these rhyolites (the KPT $\delta^{18}O$ value is slightly more "mantle-like" than those measured in Milos but similar to those of Santorini; [48]). Assuming that the asthenospheric mantle has a $\delta^{18}O$ value of ~5.3‰ [95] and accounting for a ~0.5-1‰increase due to fractional crystallization [96], some crustal material with high $\delta^{18}O$ must have participated in the generation of the KPT. However, it is uncertain (1) how much crustal material is needed ($\delta^{18}O$ of the assimilant could vary from +10 to +20; [97, 98] and lead to as little as 15% and much as 50% crustal assimilant) and (2) whether this crustal signature comes from heterogeneities contained within the slab or lithospheric mantle [99–101] and/or from the crust of the overriding plate.

As isotopic ratios remain somewhat ambiguous in quanti-

fying the relative contributions of the different reservoirs in Aegean magmas, other independent lines of evidence must be sought. Perhaps the strongest argument for a crystal fractionation dominated evolution in these magmas is results from numerical modeling of the thermal evolution of mafic magmas interacting with surrounding crust. As already discussed by Bachmann et al. (2007), these models show that mafic magmas interacting with thin (<30 km thick) crust (which is the case of the Aegean region) will lead to a very limited amount of crustal additions; the wall rocks act as containers but do not melt extensively and/or get entrained in the erupted magmas (e.g., [102, 103]).

In addition to differentiation by crystal fractionation and a limited amount of crustal assimilation, magma mixing (sensu lato) is ubiquitous (albeit not extensive) in the KPT and other magmas of the Kos-Nisyros system, as in most other magmatic provinces in the world (e.g., [104, 105]; [17, 24]). The interaction between the resident crystal-rich rhyolite and a more mafic endmember (andesite) is obvious texturally (banded pumices) and compositionally in the KPT, but only involved a small fraction of mafic magma (<20% mafic magma, based on the SiO_2 scale), as banded pumices are rare and mixing trends on compositional diagrams are limited in their extent (Figure 8). Mixing therefore played a role in creating intermediate compositions in between endmembers, but could not completely erase the obvious compositional gaps in the erupted products of the Kos-Nisyros region (Figure 8; [23, 47, 106]).

On the basis of U-Th-Pb SHRIMP dating of KPT zircons (which have no evidence for xenocrystic cores), a minimum of 250 000 years can be estimated as the time taken by the KPT magma body to reach its observed erupted volume (>60 km^3; [39]). Assuming that crystal fractionation requires ~8-10 times more basalt to produce rhyolite, at least 600 km^3 of basalt was distilled. In 300 k.y., this give a basalt flux slightly higher than 10^{-3} km^3/yr. This rate is in the low range of eruption rates estimated by [107]) for systems worldwide, consistent with the low convergence rate of the Aegean subduction zone [10].

7.2. Rejuvenated mush by gas sparging

As discussed by Keller (1969), the KPT shows obvious marks of a late reactivation event that partially resorbed quartz and feldspars. This partial resorption of the anhydrous minerals is likely to be a consequence of a reheating event that occurred shortly prior to eruption, because (1) the presence of well-developed Rapakivi textures, (2) the gradual inverse zoning in plagioclase (An content progressively increasing towards the rim) converge towards indicating a system progressively warming up prior to eruption. Textural disequilibrium in quartz and feldspars could also be due to decompression, but in such a scenario, the An content of plagioclase would be expect to drop towards the rim [84].

The reheating event, as suggested by Keller (1969), was most likely caused by underplating mafic magmas such as the one found in the banded pumices. This inference has been strengthened by the recent discovery of a deposit at the base of the KPT that contains the most mafic magma composition ever found on Kos island [108]. However, I would argue, in contrast to Keller (1969)'s scenario, that the parental silicic body was not a solidified granite, but a chemically evolved crystal mush that was still hovering above its solidus when it was reheated and partially remelted. Remelting a fully-solidified granite by intrusion of mafic magmas in the upper crust is thermally unviable [102], and would require an unreasonable amount of volatile to be transferred back to the silicic magma (as nearly all volatiles escape as magmas reach their solidii). Moreover,the granitic enclaves do not represent the unmelted protolith, as claimed by Keller (1969), but rather the crystalline margin of the magma chamber. The range of zircon U-Th-Pb ages for these enclaves are indistinguishable from those collected from pumices, which implies that they grew over the same time period (and not much before as would be expected to if the protolith was a solidified granite [39].

Based on the mineral textures and zoning patterns (mostly in feldspars), reheating was likely complex, involving several pulses of heat and chaotic stirring of the viscous mixture. It is also obvious from the different components (e.g., crystal-poor pumices and highly crystalline granitic enclaves) that parts of the magma chambers were at different temperatures. Granitic enclaves were stored near the edge of the magma body, in the colder parts of the system, while crystal-poor magma (recorded by the crystal-poor pumice) may record a higher temperature environment (although no pre-eruptive temperature estimates could be collected from these pumices due to lack of ilmenite).

The Kos Plateau Tuff magma chamber appears as a plausible case of magma rejuvenation by gas sparging from the underplating mafic layer (hot gas liberated by the mafic layer and allowed to percolate upward through the silicic crystal mush), as already suggested for other units (e.g., Fish Canyon Tuff; [109, 110], Mt St-Helens [111], Cerro Galan [112]). The reasons are the following: (1) the rejuvenated silicic magma only shows a trivial amount of magma mixing with the mafic magma, indicating that the heat transfer had to be dominated by a process other that mixing. (2) The presence of euhedral, halogen-rich biotite crystals with baryte inclusions and interlayer deficiencies (low analytical totals indicating presence of excess

H_2O) and pyrite in co-magmatic, holocrystalline granitic enclaves fragments imply that the reheating occurred at high volatile fugacities. (3) Magmas in the Kos-Nisyros volcanic centers show evidence for open-system gas fluxing through magma chambers (e.g., [54]). The continuous monitoring of the $^3He/^4He$ ratios in fumaroles of Nisyros volcano [113] showed a clear increase in $^3He/^4He$ (from 5.5 to 6.2) a couple of years after a earthquake swarm. The $^3He/^4He$ data requires a "mafic wind" reaching the surface after having crossed the shallow magmatic column.

8. Concluding remarks

The Kos Plateau Tuff is a particularly well-preserved example of a large-volume, calc-alkaline high-SiO_2 rhyolite. Its geochemical characteristics attest the importance of crystal fractionation in producing evolved magma composition the Aegean arc, which represent a relatively clean "magmatic distillation column" (very little assimilation from surrounding crust). The lack of involvement of pre-existing crust in the Aegean subduction zone (which is characterized by slow convergence rate, low magma productivity, and thin overriding continental crust) is expected from recent numerical models of basalt interaction with the continental crust [102, 103, 114].

The Kos-Nisyros area accumulated rhyolitic magmas for several hundreds of thousands of years [39] at shallow depths (~1.5-2.5 kb), and this chamber could have ended its career as a upper crustal granite. However, a period of sufficiently large intrusions of more mafic magmas reactivated the cooling crystal mush and triggered the massive KPT eruption. The limited mixing between the silicic and mafic magmas, the partial resorption of feldspars and quartz and the numerous evidence for high volatile content in the system suggest that the rejuvenation of the crystal mush was largely induced by hot gas percolation released from the mafic underplates.

The Kos-Nisyros volcanic center presents every possible signs of high magmatic unrest (earthquake swarms, hot and abundant passive degassing, active hydrothermal system; [18, 22, 113, 115, 116]). As the youngest eruption of the system (Yali rhyolite, [25]) is chemically very similar to the KPT (after a period of more mafic magmatism during the construction of the Nisyros cone), I would argue that the location should be closely monitored for future caldera-forming eruption of silicic magma.

Acknowledgements

This project was funded by the Swiss National Science Foundation (grants #2000-103441/1 and 200021-111709/1). Many thanks to Ilya Bindeman (U of Oregon) and Cedric Schnyder (Musée d'histoire naturelle de Genève) for Oxygen isotopes, Bernard Grobéty (U of Fribourg) for TEM of biotites, and Dave Wark (Rensselaer Polytechnic Institute) for very efficient help on the Ti in quartz analyses. I extent my gratitude to the International Aegean Team (from UW, Josef "The Unspunnen" Dufek, George "the pink panther" Bergantz) and from University of Geneva + Bern (Julie Bourquin, Caroline Bouvet de Maisonneuve, Alexandra Nowak, Céline Longchamp, Cédric Schnyder, Wim Degruyter, Lukas Martin, Thomas Pettke, Carl Spangler, Costanza Bonnadona Alain Burgisser, and Mike Dungan) for tasting Ouzo on some of the most beautiful terraces of the Aegean. G. Vougioukalakis and K. Kyriakopoulos were also of great help in the field. Finally, I would like to thank Chrisoula and all her family at Panorama Studios for everything they did for us.

Appendix 1

Photographs of hand samples and thin sections (epoxy colored in blue to show porosity) of all four types of pumices in the KPT.

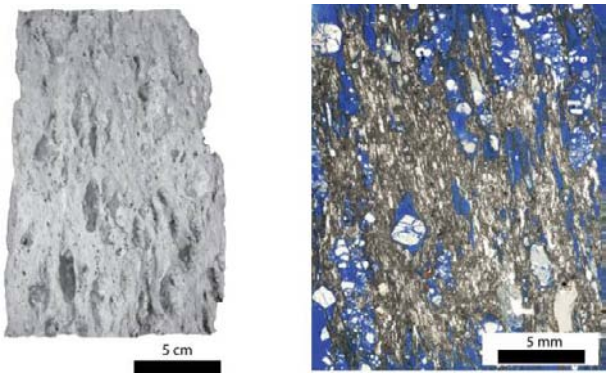

Figure 27. Tube pumice.

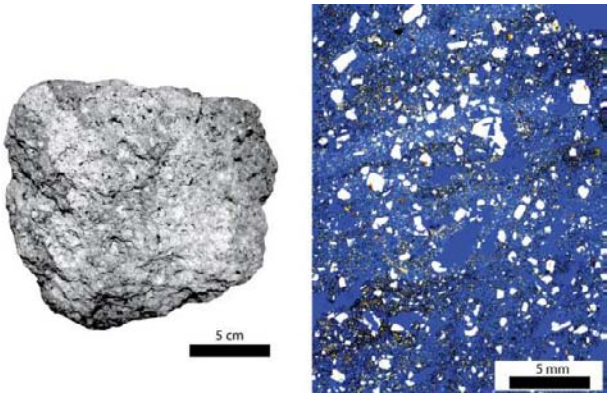

Figure 25. Banded pumice.

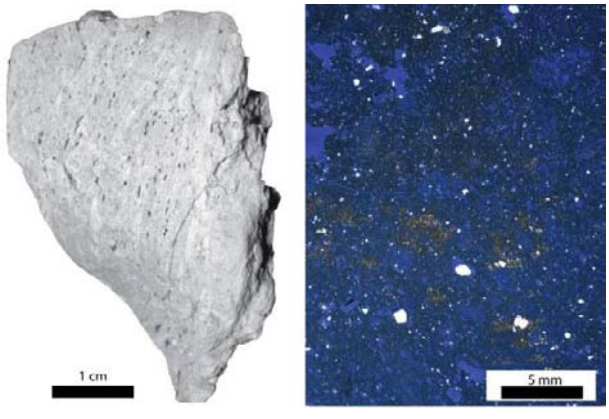

Figure 28. Microvesicular, crystal-poor pumice.

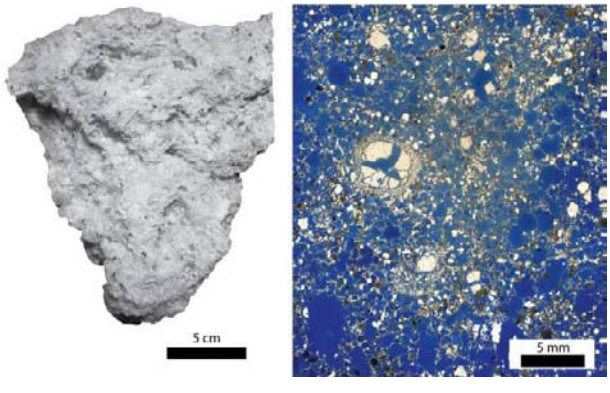

Figure 26. Frothy pumice.

Appendix 2

Full table including all whole-rock XRF and ICPMS analyses.

Table 3. XRF and ICPMS data for whole-rock samples of the KPT.

	KPT04_35	KPT05-11	KPT05-8	KPT06-43a	KPT06-43b	KPT04_3	KPT04_5	KPT05-12
Descript.	Xtal-poor pum.	Xtal-poor D	Xtal-poor	Big xtalpoor	Big xtalpoor	Pumice	Pumice	Frothy, D
Unit	B	D	B	B	B	D	D	D
Location	Kardamena	Aegean Village	Aegean Village	Aegean Village	Aegean Village	Kardamena	Kardamena	Aegean Village
SiO_2	74.68	75.07	74.01	74.60	74.57	75.74	74.14	74.48
TiO_2	0.21	0.18	0.20	0.19	0.19	0.20	0.20	0.18
Al_2O3	14.07	13.80	13.61	13.73	13.75	13.65	14.65	14.07
Fe_2O_3	1.33	1.25	1.42	1.36	1.34	1.24	1.19	1.23
MnO	0.06	0.06	0.06	0.06	0.06	0.05	0.05	0.06
MgO	0.49	0.40	0.78	0.47	0.47	0.37	0.35	0.36
CaO	1.68	1.30	2.10	1.77	1.76	1.38	1.52	1.31
Na_2O	3.54	3.85	3.79	3.70	3.73	3.73	4.11	4.18
K_2O	3.92	4.02	3.99	4.07	4.08	3.61	3.77	4.06
P_2O_5	0.02	0.07	0.05	0.05	0.05	0.02	0.02	0.07
Somme	100	100	100	100	100	100	100	100
LOI	2.11	3.21	2.12	2.10	2.29	2.39	2.49	3.38
Nb	18	19	18	19	19	18	17	20
Zr	83	79	84	84	85	83	70	71
Y	13	12	13	13	13	12	12	13
Sr	152	156	152	156	156	145	163	143
U	< 2 <	< 2 <	< 2 <	2	< 2 <	< 2 <	< 2 <	< 2 <
Rb	110	116	112	112	113	104	105	116
Th	12	12	11	13	12	12	10	11
Pb	9	11	11	11	11	9	9	10
Ga	14	14	12	14	14	14	14	14
Zn	23	25	28	24	23	23	19	22
Ni	3	7	5	4	4	3	3	4
Cr	7	15	8	4	4	< 2 <	5	3
V	11	8	12	12	11	8	6	7
Ce	51	45	45	49	50	44	40	28
Ba	874	876	836	902	892	701	689	615
La	29	47	26	27	29	25	23	39

	KPT05-30	KPT05-30	KPT05-33	KPT05-34	KPT05-35	KPT05-7	KPT04_4	KPT04_19
Descript.	Frothy, D	Frothy pumice	Frothy pumice	Frothy pumice	Frothy pumice	Tube, B	Pumices	Pumice
Unit	D	D	D	D	D	B	B	E
Location	Aegean Village	Aegean Village	Aegean Village	Aegean Village	Aegean Village	Aegean Village	Kardamena	Andi. Quarry
SiO_2	73.98	73.76	74.90	74.89	74.05	74.96	74.50	75.03
TiO_2	0.18	0.20	0.18	0.18	0.18	0.18	0.21	0.20
Al_2O_3	14.39	14.25	13.85	13.64	14.41	13.74	14.47	14.13
Fe_2O_3	1.31	1.49	1.22	1.27	1.23	1.29	1.32	1.21
MnO	0.06	0.06	0.06	0.06	0.06	0.06	0.06	0.05
MgO	0.35	0.40	0.37	0.40	0.37	0.38	0.36	0.32
CaO	1.39	1.34	1.32	1.34	1.46	1.31	1.47	1.34
Na_2O	4.32	4.34	4.15	4.09	4.32	3.97	3.87	3.49
K_2O	3.97	4.11	3.91	4.08	3.88	4.09	3.73	4.19
P_2O_5	0.04	0.05	0.04	0.04	0.05	0.04	0.02	0.03
Somme	100	100	100	100	100	100	100	100
LOI	3.18	2.64	2.75	2.34	2.53	2.77	2.45	2.27
Nb	20	20	20	18	19	19	19	18
Zr	78	99	82	83	73	78	81	81
Y	14	14	13	13	12	13	13	13
Sr	148	145	142	156	164	141	152	148
U	< 2 <	2	3	< 2 <	2	2	< 2 <	< 2 <
Rb	117	120	115	114	113	113	118	114
Th	13	13	12	12	12	12	11	12
Pb	10	10	10	10	9	10	9	9
Ga	14	13	12	14	14	14	14	14
Zn	20	22	23	23	22	22	24	21
Ni	2	2	15	3	6	3	6	7
Cr	14	7	< 2 <	3	< 2 <	< 2 <	2	3
V	5	10	7	10	7	6	8	8
Ce	44	44	43	45	41	36	44	47
Ba	520	658	598	901	688	597	607	904
La	41	26	27	24	25	49	24	25

	KPT04_21	KPT04_23	KPT04_24	KPT04_28	KPT04_40	KPT04_10	KPT04_17	KPT05-15
Descript.	Pumice	Pumice	Pumice	Pumice	Pumice	Pumice	Pumice	Pumice
Unit	E	E	E	E	E	E	Top of E	F
Location	Trop. Beach	Pothia	Pothia	Golden Beach	Tilos	Andi. Castle	La Plata quarry	Plaka
SiO_2	75.51	75.67	75.18	74.39	73.38	75.80	75.03	76.25
TiO_2	0.21	0.21	0.21	0.20	0.22	0.18	0.20	0.18
Al_2O_3	13.73	13.68	13.97	14.55	14.29	13.79	14.15	13.10
Fe_2O_3	1.30	1.24	1.28	1.24	1.36	0.96	1.24	1.20
MnO	0.06	0.05	0.06	0.06	0.06	0.06	0.05	0.06
MgO	0.37	0.34	0.34	0.34	0.53	0.18	0.34	0.34
CaO	1.37	1.36	1.36	1.36	1.65	0.93	1.43	1.13
Na_2O	3.52	3.45	3.36	3.75	4.09	3.59	3.75	3.59
K_2O	3.88	3.97	4.21	4.08	4.38	4.50	3.78	4.14
P_2O_5	0.05	0.03	0.02	0.01	0.03	0.01	0.02	0.03
Somme	100	100	100	100	100	100	100	100
LOI	2.00	1.79	1.74	2.41	3.40	3.29	2.42	2.86
Nb	18	18	19	19	19	18	18	19
Zr	85	77	85	80	82	90	83	76
Y	12	13	13	13	13	12	13	14
Sr	145	146	144	149	147	110	151	126
U	4	< 2 <	< 2 <	4	< 2 <	2	< 2 <	2
Rb	117	106	115	113	114	111	108	114
Th	13	12	12	13	12	15	11	12
Pb	9	9	10	9	10	11	9	9
Ga	13	13	14	14	14	13	14	14
Zn	24	21	23	20	20	23	21	21
Ni	14	3	3	4	2	3	8	8
Cr	< 2 <	23	< 2 <	< 2 <	< 2 <	< 2 <	< 2 <	3
V	9	8	8	7	7	3	9	7
Ce	44	47	51	46	48	61	44	39
Ba	795	776	727	817	713	888	606	613
La	25	26	32	25	24	37	26	35

	KPT04_12	KPT04_36	KPT05-3	KPT05-14	KPT05-26	KPT04_8	KPT04_15	KPT04_20
Descript.	Pumice w/inc.	Banded pumice	Banded, E	Banded	Grey, Xtal-poor, B	Granitoid	Granitoid	Granitoid
Unit	E	E	E	Block	B	Ebx	E	E
Location	Andi. Quarry	Kardamena	Andimahia Quarry	Sunny Beach	Aegean Village	Andi. Castle	Ag. Theologos	Trop. Beach
SiO_2	74.41	71.75	71.29	72.52	73.59	73.52	76.13	73.26
TiO_2	0.20	0.28	0.34	0.25	0.19	0.20	0.17	0.22
Al_2O_3	14.55	14.72	14.55	14.52	13.85	15.04	13.69	15.17
Fe_2O_3	1.25	1.87	2.41	1.75	1.34	1.15	0.84	1.25
MnO	0.05	0.06	0.07	0.06	0.06	0.03	0.03	0.05
MgO	0.32	0.90	1.03	0.80	0.70	0.32	0.20	0.39
CaO	1.38	2.95	2.88	2.11	2.16	1.38	0.87	1.47
Na_2O	3.40	3.64	3.64	3.82	3.91	4.14	3.65	4.27
K_2O	4.43	3.82	3.70	4.10	4.15	4.16	4.42	3.91
P_2O_5	0.00	0.01	0.09	0.07	0.05	0.03	0.01	0.01
Somme	100	100	100	100	100	100	100	100
LOI	2.12	2.28	2.43	2.87	3.26	0.10	0.07	0.19
Nb	19	18	18	18	17	16	17	18
Zr	85	90	95	83	78	76	76	83
Y	13	14	15	14	12	11	16	13
Sr	153	194	226	185	149	163	92	169
U	< 2 <	< 2 <	< 2 <	< 2 <	2	< 2 <	2	1
Rb	112	101	97	103	105	103	100	113
Th	12	11	11	11	11	9	12	12
Pb	10	9	10	9	11	9	12	10
Ga	14	14	15	14	13	14	14	15
Zn	26	29	31	25	30	11	7	14
Ni	10	7	10	12	3	2	< 2 <	6
Cr	< 2 <	20	5	5	5	11	< 2 <	< 2 <
V	8	21	32	17	9	8	5	9
Ce	49	47	40	33	47	41	33	47
Ba	859	796	734	762	791	1108	723	1068
La	25	26	30	41	24	18	16	24

	KPT04_29	KPT04_37	KPT05-4
Descript.	Granitoid	Granitoid	Granitoid
Unit	E	Ebx	E
Location	Golden Beach	EKO plant	Ag. Theologos
SiO_2	76.23	74.72	77.18
TiO_2	0.17	0.19	0.11
Al_2O_3	13.43	14.40	12.80
Fe_2O_3	0.82	1.11	0.56
MnO	0.02	0.03	0.02
MgO	0.22	0.29	0.13
CaO	0.71	1.26	0.56
Na_2O	3.58	3.89	3.69
K_2O	4.78	4.09	4.92
P_2O_5	0.04	0.03	0.03
Somme	100	100	100
LOI	0.07	0.11	0.09
Nb	22	14	23
Zr	59	73	47
Y	13	11	13
Sr	58	143	46
U	2	3	< 2 <
Rb	100	119	115
Th	11	5	9
Pb	10	10	13
Ga	13	14	14
Zn	7	12	5
Ni	2	2	< 2 <
Cr	< 2 <	< 2 <	4
V	6	9	< 2 <
Ce	29	42	14
Ba	518	959	409
La	17	23	17

Table 4. ICPMS trace element data on KPT samples.

	KPT04_4 (Tube B)	KPT04_19 (Tube E)	KPT05_15 (Tube F)	KPT05_4 (Hol Gra)
Be	2.39	2.81	2.73	2.36
Sc	2.95	2.86	2.76	2.40
V	17.32	17.05	16.23	10.07
Cr	84.38	245.47	231.50	67.74
Co	2.16	2.97	1.59	0.35
Ni	6.45	6.82	6.98	0.56
Cu	7.55	14.30	10.47	3.96
Zn	32.74	41.23	20.96	6.26
Ga	47.84	62.14	43.04	28.93
Rb	106.88	104.93	100.94	92.93
Sr	155.14	150.58	115.77	38.94
Y	13.24	12.10	12.63	13.29
Zr	88.33	83.24	80.17	55.73
Nb	17.00	16.82	15.92	20.29
Cs	3.48	3.33	3.25	0.73
Ba	623.40	920.20	595.56	325.29
La	30.76	28.84	27.44	14.73
Ce	49.50	45.60	42.98	25.25
Pr	4.34	4.07	3.84	2.36
Nd	13.28	12.99	11.65	7.47
Sm	2.08	2.01	2.19	1.54
Eu	0.39	0.40	0.37	0.17
Gd	1.62	1.76	1.91	1.35
Tb	0.29	0.26	0.26	0.27
Dy	1.86	1.84	1.75	1.90
Ho	0.37	0.39	0.39	0.40
Er	1.20	1.22	1.17	1.30
Tm	0.20	0.19	0.20	0.21
Yb	1.60	1.56	1.47	1.62
Lu	0.22	0.22	0.22	0.26
Hf	2.46	2.21	2.30	2.11
Ta	1.43	1.44	1.34	1.88
Pb	16.12	9.51	9.46	14.66
Th	13.85	13.11	12.57	12.18
U	4.00	3.97	3.72	3.12

Appendix 3

Corrugated and fragile biotites in KPT samples (pumices and granitic clasts).

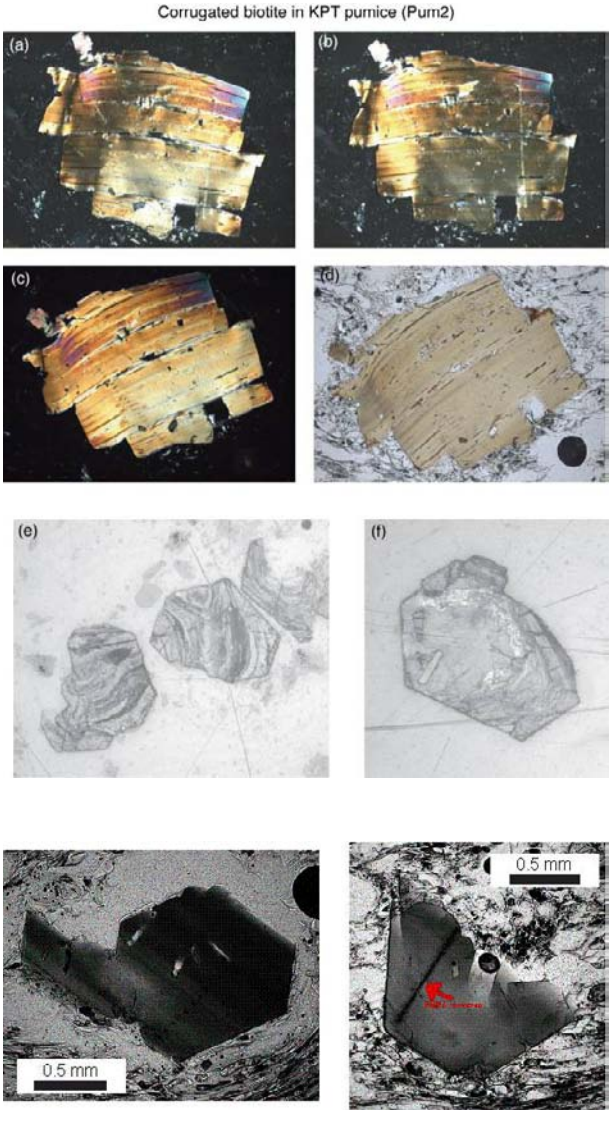

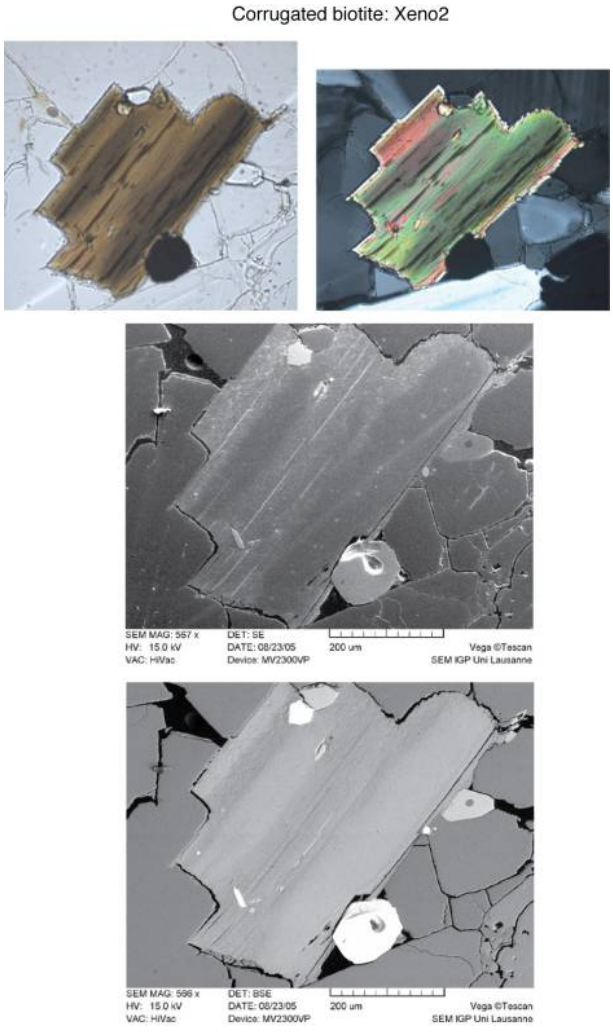

Figure 30. Biotite crystals from KPT tube pumice samples showing bands of variable shades of brown in natural light, and holes in areas hit by the electron beam during an e-probe analysis (at normal analytical conditions, 15 kV and 15 nA).

Appendix 4

HR-TEM technical details and data from the Kos Plateau Tuff biotite.

Method: Biotite flakes hand-picked a fresh Kos Plateau Tuff pumice (KPT04-2) were placed on a carbon grid with a drop of ethanol dispersion and dried in air. TEM analyses were performed at the University of Fribourg (Switzerland) using a Philips CM200 operated at 200 kV, equipped with an EDAX energy dispersive X-ray spectrometer (EDS). The beam diameter for the EDS analyses was 5 nm.

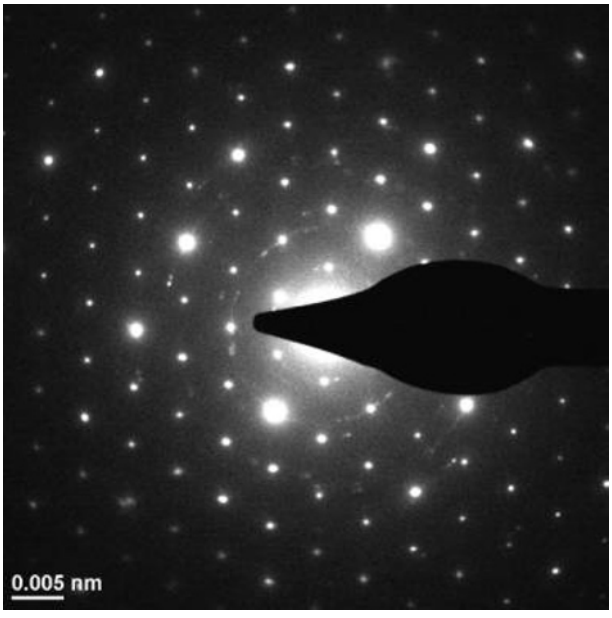

Figure 32. The selected plane (001) shows a pattern of phyllosilicate, and can be indexed as biotite. The small circular reflections seen along side with the main biotite reflections are from smaller biotite flakes lying on the main grain.

Appendix 5

Full spreadsheet of Quartz Ti profiles by electron microprobe (done at Rensselaer Polytechnic Institute).

Table 5. Ti concentrations in quartz of the KPT (Electron microprobe traverses).

Label	PPM Ti	Activity Ti = 0.9	Activity Ti = 0.8	Activity Ti = 0.7	Activity Ti = 0.6	Activity Ti = 0.5
KPT21-2	52	690.61	702.67	716.25	732.34	752.47
KPT21-2	64	711.27	723.82	738.00	754.82	775.92
KPT21-2	58	702.01	714.34	728.25	744.75	765.41
KPT21-2	57	700.59	712.88	726.75	743.20	763.79
KPT21-2	61	706.28	718.71	732.75	749.40	770.26
KPT21-2	63	710.56	723.09	737.25	754.05	775.11
KPT21-2	56	697.74	709.96	723.75	740.09	760.55
KPT21-2	63	710.56	723.09	737.25	754.05	775.11
KPT21-2	56	697.74	709.96	723.75	740.09	760.55
KPT21-2	55	697.02	709.24	723.00	739.32	759.74
KPT21-2	59	704.15	716.53	730.50	747.07	767.83
KPT21-2	55	697.02	709.24	723.00	739.32	759.74
KPT21-2	59	702.72	715.07	729.00	745.52	766.21
KPT21-2	54	695.60	707.78	721.50	737.77	758.13
KPT21-2	65	712.69	725.28	739.50	756.37	777.54
KPT21-2	65	712.69	725.28	739.50	756.37	777.54
KPT21-2	70	721.24	734.02	748.50	765.67	787.24
KPT21-2	64	711.98	724.55	738.75	755.60	776.73
KPT21-2	65	713.41	726.00	740.25	757.15	778.34
KPT21-2	67	717.68	730.38	744.75	761.80	783.20
Average T		705.68	718.09	732.11	748.74	769.57
KPT21-3	56	698.45	710.69	724.50	740.87	761.36
KPT21-3	50	687.76	699.76	713.25	729.24	749.23
KPT21-3	52	691.33	703.40	717.00	733.12	753.28
KPT21-3	54	695.60	707.78	721.50	737.77	758.13
KPT21-3	54	695.60	707.78	721.50	737.77	758.13
KPT21-3	49	686.34	698.30	711.75	727.69	747.61
KPT21-3	48	684.91	696.84	710.25	726.14	746.00
KPT21-3	55	697.02	709.24	723.00	739.32	759.74
KPT21-3	47	683.49	695.38	708.75	724.59	744.38
KPT21-3	47	682.78	694.65	708.00	723.82	743.57
KPT21-3	56	697.74	709.96	723.75	740.09	760.55
KPT21-3	50	687.76	699.76	713.25	729.24	749.23

continued on next page

Label	PPM Ti	Activity Ti = 0.9	Activity Ti = 0.8	Activity Ti = 0.7	Activity Ti = 0.6	Activity Ti = 0.5
KPT21-3	52	692.04	704.13	717.75	733.89	754.08
KPT21-3	58	701.30	713.61	727.50	743.97	764.60
KPT21-3	47	682.07	693.93	707.25	723.04	742.76
KPT21-3	59	704.15	716.53	730.50	747.07	767.83
KPT21-3	54	695.60	707.78	721.50	737.77	758.13
KPT21-3	60	705.57	717.98	732.00	748.62	769.45
KPT21-3	52	691.33	703.40	717.00	733.12	753.28
KPT21-3	58	702.01	714.34	728.25	744.75	765.41
Average T		693.14	705.26	718.91	735.10	755.34
KPT21-3B	48	684.91	696.84	710.25	726.14	746.00
KPT21-3B	57	700.59	712.88	726.75	743.20	763.79
KPT21-3B	60	704.86	717.26	731.25	747.85	768.64
KPT21-3B	70	721.95	734.75	749.25	766.45	788.05
KPT21-3B	63	710.56	723.09	737.25	754.05	775.11
KPT21-3B	66	715.54	728.19	742.50	759.47	780.77
KPT21-3B	71	724.09	736.94	751.50	768.78	790.47
KPT21-3B	74	729.08	742.04	756.75	774.20	796.13
KPT21-3B	74	729.08	742.04	756.75	774.20	796.13
KPT21-3B	76	731.93	744.96	759.75	777.30	799.37
Average T		715.26	727.90	742.20	759.16	780.45
KPT21-4	51	689.90	701.95	715.50	731.57	751.66
KPT21-4	69	720.53	733.29	747.75	764.90	786.43
KPT21-4	54	694.89	707.05	720.75	736.99	757.32
KPT21-4	59	702.72	715.07	729.00	745.52	766.21
KPT21-4	66	714.83	727.46	741.75	758.70	779.96
KPT21-4	65	712.69	725.28	739.50	756.37	777.54
KPT21-4	57	699.16	711.42	725.25	741.65	762.17
KPT21-4	65	713.41	726.00	740.25	757.15	778.34
KPT21-4	65	712.69	725.28	739.50	756.37	777.54
KPT21-4	54	695.60	707.78	721.50	737.77	758.13
KPT21-4	61	707.00	719.44	733.50	750.17	771.07
KPT21-4	68	719.10	731.84	746.25	763.35	784.81
KPT21-4	65	713.41	726.00	740.25	757.15	778.34
KPT21-4	67	716.97	729.65	744.00	761.02	782.39
KPT21-4	63	709.85	722.36	736.50	753.27	774.30
KPT21-4	57	699.87	712.15	726.00	742.42	762.98
KPT21-4	58	701.30	713.61	727.50	743.97	764.60
KPT21-4	67	716.26	728.92	743.25	760.25	781.58
KPT21-4	57	699.16	711.42	725.25	741.65	762.17
KPT21-4	55	697.02	709.24	723.00	739.32	759.74
KPT21-4	63	710.56	723.09	737.25	754.05	775.11
KPT21-4	71	724.09	736.94	751.50	768.78	790.47
Average T		707.77	720.24	734.32	751.02	771.95

continued on next page

Label	PPM Ti	Activity Ti = 0.9	Activity Ti = 0.8	Activity Ti = 0.7	Activity Ti = 0.6	Activity Ti = 0.5
KPT21-5	54	694.17	706.32	720.00	736.22	756.51
KPT21-5	61	707.00	719.44	733.50	750.17	771.07
KPT21-5	61	707.00	719.44	733.50	750.17	771.07
KPT21-5	n.d.					
KPT21-5	52	690.61	702.67	716.25	732.34	752.47
KPT21-5	57	699.87	712.15	726.00	742.42	762.98
KPT21-5	49	685.63	697.57	711.00	726.92	746.81
KPT21-5	55	697.02	709.24	723.00	739.32	759.74
KPT21-5	51	689.90	701.95	715.50	731.57	751.66
KPT21-5	59	702.72	715.07	729.00	745.52	766.21
KPT21-5	67	717.68	730.38	744.75	761.80	783.20
KPT21-5	78	734.78	747.88	762.75	780.40	802.60
KPT21-5	73	727.65	740.59	755.25	772.65	794.52
KPT21-5	49	685.63	697.57	711.00	726.92	746.81
KPT21-5	72	726.23	739.13	753.75	771.10	792.90
Average T		704.71	717.10	731.09	747.68	768.47
KPT35-1 LINE 1	63	710.56	723.09	737.25	754.05	775.11
KPT35-1 LINE 1	57	700.59	712.88	726.75	743.20	763.79
KPT35-1 LINE 1	52	690.61	702.67	716.25	732.34	752.47
KPT35-1 LINE 1	55	696.31	708.51	722.25	738.54	758.94
KPT35-1 LINE 1	55	697.02	709.24	723.00	739.32	759.74
KPT35-1 LINE 1	57	699.87	712.15	726.00	742.42	762.98
KPT35-1 LINE 1	68	719.10	731.84	746.25	763.35	784.81
KPT35-1 LINE 1	66	715.54	728.19	742.50	759.47	780.77
KPT35-1 LINE 1	46	681.35	693.20	706.50	722.27	741.95
KPT35-1 LINE 1	53	693.46	705.59	719.25	735.44	755.70
Average T		700.44	712.74	726.60	743.04	763.63
KPT35-1 LINE 2	58	702.01	714.34	728.25	744.75	765.41
KPT35-1 LINE 2	52	690.61	702.67	716.25	732.34	752.47
KPT35-1 LINE 2	51	689.19	701.22	714.75	730.79	750.85
KPT35-1 LINE 2	58	701.30	713.61	727.50	743.97	764.60
KPT35-1 LINE 2	65	713.41	726.00	740.25	757.15	778.34
KPT35-1 LINE 2	56	697.74	709.96	723.75	740.09	760.55
KPT35-1 LINE 2	53	693.46	705.59	719.25	735.44	755.70
KPT35-1 LINE 2	59	702.72	715.07	729.00	745.52	766.21
KPT35-1 LINE 2	55	696.31	708.51	722.25	738.54	758.94
KPT35-1 LINE 2	46	681.35	693.20	706.50	722.27	741.95
KPT35-1 LINE 2	55	697.02	709.24	723.00	739.32	759.74
KPT35-1 LINE 2	53	692.75	704.86	718.50	734.67	754.89
KPT35-1 LINE 2	52	692.04	704.13	717.75	733.89	754.08
Average T		696.15	708.34	722.08	738.37	758.75
KPT35-2	58	702.01	714.34	728.25	744.75	765.41
KPT35-2	63	710.56	723.09	737.25	754.05	775.11

continued on next page

Label	PPM Ti	Activity Ti = 0.9	Activity Ti = 0.8	Activity Ti = 0.7	Activity Ti = 0.6	Activity Ti = 0.5
KPT35-2	60	705.57	717.98	732.00	748.62	769.45
KPT35-2	50	688.48	700.49	714.00	730.02	750.04
KPT35-2	57	700.59	712.88	726.75	743.20	763.79
KPT35-2	53	692.75	704.86	718.50	734.67	754.89
KPT35-2	63	710.56	723.09	737.25	754.05	775.11
KPT35-2	51	689.90	701.95	715.50	731.57	751.66
KPT35-2	59	702.72	715.07	729.00	745.52	766.21
KPT35-2	62	708.42	720.90	735.00	751.72	772.68
KPT35-2	57	700.59	712.88	726.75	743.20	763.79
KPT35-2	62	707.71	720.17	734.25	750.95	771.87
KPT35-2	60	704.86	717.26	731.25	747.85	768.64
KPT35-3	57	699.16	711.42	725.25	741.65	762.17
KPT35-3	57	699.87	712.15	726.00	742.42	762.98
KPT35-3	51	689.19	701.22	714.75	730.79	750.85
KPT35-3	50	688.48	700.49	714.00	730.02	750.04
KPT35-3	64	711.27	723.82	738.00	754.82	775.92
KPT35-3	60	705.57	717.98	732.00	748.62	769.45
KPT35-3	59	704.15	716.53	730.50	747.07	767.83
KPT35-3	67	717.68	730.38	744.75	761.80	783.20
KPT35-3	76	731.93	744.96	759.75	777.30	799.37
KPT35-3	75	731.21	744.23	759.00	776.53	798.56
KPT35-3	71	724.09	736.94	751.50	768.78	790.47
KPT35-3	65	713.41	726.00	740.25	757.15	778.34
KPT35-3	71	723.38	736.21	750.75	768.00	789.67
Average T		706.31	718.74	732.78	749.43	770.29
KPT2-4	66	715.54	728.19	742.50	759.47	780.77
KPT2-4	72	724.80	737.67	752.25	769.55	791.28
KPT2-4	59	703.43	715.80	729.75	746.30	767.02
KPT2-4	63	709.85	722.36	736.50	753.27	774.30
KPT2-4	52	690.61	702.67	716.25	732.34	752.47
KPT2-4	57	700.59	712.88	726.75	743.20	763.79
KPT2-4	55	696.31	708.51	722.25	738.54	758.94
KPT2-4	56	697.74	709.96	723.75	740.09	760.55
KPT2-4	60	704.86	717.26	731.25	747.85	768.64
KPT2-4	62	708.42	720.90	735.00	751.72	772.68
KPT2-4	67	716.26	728.92	743.25	760.25	781.58
KPT2-4	53	693.46	705.59	719.25	735.44	755.70
Average T		705.16	717.56	731.56	748.17	768.98
KPT21-5	59	703.43	715.80	729.75	746.30	767.02
KPT21-5	72	725.52	738.40	753.00	770.33	792.09
KPT21-5	66	714.83	727.46	741.75	758.70	779.96
KPT21-5	64	711.98	724.55	738.75	755.60	776.73
KPT21-5	58	701.30	713.61	727.50	743.97	764.60
KPT21-5	62	708.42	720.90	735.00	751.72	772.68

continued on next page

Label	PPM Ti	Activity Ti = 0.9	Activity Ti = 0.8	Activity Ti = 0.7	Activity Ti = 0.6	Activity Ti = 0.5
KPT21-5	55	697.02	709.24	723.00	739.32	759.74
KPT21-5	62	708.42	720.90	735.00	751.72	772.68
KPT21-5	63	710.56	723.09	737.25	754.05	775.11
KPT21-5	63	709.85	722.36	736.50	753.27	774.30
KPT21-5	63	709.85	722.36	736.50	753.27	774.30
KPT21-5	65	713.41	726.00	740.25	757.15	778.34
KPT21-5	54	694.17	706.32	720.00	736.22	756.51
KPT21-5	57	700.59	712.88	726.75	743.20	763.79
KPT21-5	67	716.26	728.92	743.25	760.25	781.58
KPT21-5	63	710.56	723.09	737.25	754.05	775.11
KPT21-5	60	705.57	717.98	732.00	748.62	769.45
KPT21-5	83	744.75	758.08	773.25	791.25	813.93
KPT21-5	71	724.09	736.94	751.50	768.78	790.47
KPT21-5	61	707.00	719.44	733.50	750.17	771.07
KPT21-5	60	705.57	717.98	732.00	748.62	769.45
KPT21-5	66	714.83	727.46	741.75	758.70	779.96
KPT21-5	67	716.97	729.65	744.00	761.02	782.39
KPT21-5	63	709.85	722.36	736.50	753.27	774.30
KPT21-5	71	724.09	736.94	751.50	768.78	790.47
Average T		711.55	724.11	738.30	755.13	776.24

References

[1] Wilson C.J.N., Supereruptions and supervolcanoes: processes and products, Elements 4, 2008, 29-34

[2] Woo G., The Mathematics of Natural Catastrophes, Imperial College Press, London, 1999

[3] Sparks R.S.J., Self S., Grattan J., Oppenheimer C., Pyle D.M., Rymer H., Super-eruptions: global effects and future threats., The Geological Society of London, London, UK, 2005

[4] Keller J., Origin of rhyolites by anatectic melting of granitic crustal rocks; the example of rhyolitic pumice from the island of Kos (Aegean sea), Bulletin Volcanologique 33, 1969, 942-959

[5] Keller J., Mediterranean island arcs, in: R.S. Thorpe, (Ed.), Andesites, John Wiley & Sons, Chichester, United Kingdom, 1982, 307-325

[6] Wortel M.J.R., Spakman W., Subduction and slab detachment in the Mediterranean-Carpathian Region, Science 290, 2000, 1910-1917

[7] Jolivet L., A comparison of geodetic and finite strain pattern in the Aegean, geodynamic implications, Earth and Planetary Science Letters 187, 2001, 95-104

[8] LePichon X., Angelier J., The hellenic arc and trench system: A key to the Neotectonic evolution of the Eastern Mediterrenean area, Tectonophysics 60, 1979, 1-42

[9] Papadopoulos G.A., Kondopoulou D.P., Leventakis G.-A., Pavlides S.B., Seismotectonics of the Aegean region, Tectonophysics 124, 1986, 67-84

[10] Jackson J., Rates of active deformation in the Eastern Mediterranean, in: E. Boschi, et al., (Ed.), Recent Evolution and Seismicity of the Mediterranean Region, Kluwer, Dordrecht, 1993, 53-64

[11] Hughes G.R., Mahood G.A., Tectonic controls on the nature of large silicic calderas in volcanic arcs, Geology 36, 2008, 627-630

[12] Matsuda J., Senoh K., Maruoka T., Sato H., Mitropolous P., K-Ar ages of the Aegean volcanic rocks and their implication for the arc-trench system, Geochemical Journal 33, 1999, 369-377

[13] Fytikas M., Giuliani O., Innocenti F., Marinelli G., Mazzuoli R., Geochronological data on recent magmatism of the Aegean Sea, Tectonophysics 31, 1976, 129-134

[14] Bellon H., Jarrige J.J., L'activité magmatique néogene et quaternaire dans l'ile de Kos, Greece: Données radio chronologiques, C.R. Acad. Sci. Paris 288, 1979

[15] Pasteels P., Kolios N., Boven A., Saliba E., Applicability of the K/Ar method to whole-rock samples

of acid lava and pumice: Case of the Upper Pleistocene domes and pyroclasts on Kos Island, Aegean Sea, Greece, Chemical Geology 57, 1986, 145-154
[16] Allen S.R., Reconstruction of a major caldera-forming eruption from pyroclastic deposit characteristics: Kos Plateau Tuff, eastern Aegean Sea, Journal of Volcanology and Geothermal Research 105, 2001, 141-162
[17] Francalanci L., Varekamp J.C., Vougioukalakis G., Defant M.J., Innocenti F., Manetti P., Crystal retention, fractionation and crustal assimilation in a convecting magma chamber, Nisyros Volcano, Greece, Bulletin of Volcanology 56, 1995, 601-620
[18] Groceix M.H., Sur l'état du volcan de Nisyros au mois de mars 1873, Compte Rendu Séances Acad. Sci. Paris LXXVII, 1873, 597-601
[19] Di Paola G.M., Volcanology and Petrology of Nisyros Island (Dodecanese, Greece), Bulletin of Volcanology 38, 1974, 944-987
[20] Wyers G.P., Barton M., Polybaric evolution of calc-alkaline magmas from Nisyros, southeastern Hellenic Arc, Greece, Journal of Petrology 30, 1989, 1-37
[21] Limburg E.M., Varekamp J.C., Young pumice deposits on Nisyros, Greece, Bulletin of Volcanology 54, 1991, 68-77
[22] Brombach T., Caliro S., Chiodini G., Fiebig J., Hunziker J., Raco B., Geochemical evidence for mixing of magmatic fluids with seawater, Nisyros hydrothermal system, Greece, Bulletin of Volcanology 65, 2003, 505-516
[23] Buettner A., Kleinhanns I.C., Rufer D., Hunziker J.C., Villa I.M., Magma generation at the easternmost section of the Hellenic arc: Hf, Nd, Pb and Sr isotope geochemistry of Nisyros and Yali volcanoes (Greece), Lithos 83, 2005, 29-46
[24] Zellmer G.F., Turner S.P., Arc dacite genesis pathways: Evidence from mafic enclaves and their hosts in Aegean lavas, Lithos 95, 2007, 346-362
[25] Allen S.R., McPhie J., Water-settling and resedimentation of submarine rhyolitic pumice at Yali, eastern Aegean, Greece, Journal of Volcanology and Geothermal Research 95, 2000, 285-307
[26] Papanikolaou D.J., Lykousis N.P.V., Submarine reconnaissance, Newsletter of the European Centre on Prevention and Forecasting of Earthquakes, ECPFE and EPPO 2, 1998, 23-26
[27] Pfeifer H.R., Lavanchy J.C., Serneels V., Bulk chemical and industrial materials by X-Ray Fluorescence, recent developments and aplication to material rich in iron oxides, Journal of Trace MicroprobeTechniques 9, 1991, 127-147
[28] Wark D.A., Hildreth W., Spear F.S., Cherniak D.J., Watson E.B., Pre-eruption recharge of the Bishop magma system, Geology 35, 2007, 235-238
[29] Rodriguez C., Selles D., Dungan M., Langmuir C., Leeman W., Adakitic Dacites Formed by Intracrustal Crystal Fractionation of Water-rich Parent Magmas at Nevado de Longavi Volcano (36{middle dot}2{degrees}S; Andean Southern Volcanic Zone, Central Chile), J. Petrology 48, 2007, 2033-2061
[30] Bindeman I., Gurenko A., Sigmarsson O., Chaussidon M., Oxygen isotope heterogeneity and disequilibria of olivine crystals in large volume Holocene basalts from Iceland: Evidence for magmatic digestion and erosion of Pleistocene hyaloclastites, Geochimica et Cosmochimica Acta 72, 2008, 4397-4420
[31] Stadlbauer E., Vulkanologishe-geochemische Analyse eines jungen Ignimbrites: Der Kos-Plateau-Tuff (Südost-Ägäis), PhD, Freiburg, 1988
[32] Smith P.E., Evensen N.M., York D., Under the volcano; a new dimension in Ar-Ar dating of volcanic ash, Geophysical Research Letters 27, 2000, 585-588
[33] Smith P.E., York D., Chen Y., Evensen N.M., Single crystal $^{40}Ar/^{39}Ar$ dating of a late Quaternary paroxysm on Kos, Greece; concordance of terrestrial and marine ages, Geophysical Research Letters 23, 1996, 3047-3050
[34] Allen S.R., Cas R.A.F., Rhyolitic fallout and pyroclastic density current deposits from a phreatoplinian eruption in the eastern Aegean Sea, Greece, Journal of Volcanology and Geothermal Research 86, 1998, 219-251
[35] Allen S.R., Cas R.A.F., Lateral variations within coarse co-ignimbrite lithic breccias of the Kos Plateau Tuff, Greece, Bulletin of Volcanology 59, 1998, 356-377
[36] Allen S.R., Stadlbauer E., Keller J., Stratigraphy of the Kos Plateau Tuff: product of a major Quaternary explosive rhyolitic eruption in the eastern Aegean, Greece, International Journal of Earth Sciences 88, 1999, 132-156
[37] Allen S.R., Cas R.A.F., Transport of pyroclastic flows across the sea during the explosive, rhyolitic eruption of the Kos Plateau Tuff, Greece, Bulletin of Volcanology 62, 2001, 441-456
[38] Allen S.R., McPhie, Syn-eruptive chaotic breccia on Kos, Greece, associated with an energetic pyroclastic flow, Bulletin of Volcanology 63, 2001, 421-432
[39] Bachmann O., Charlier B.L.A., Lowenstern J.B., Zircon crystallization and recycling in the magma chamber of the rhyolitic Kos Plateau Tuff (Aegean Arc), Geology 35, 2007, 73-76
[40] Bouvet de Maisonneuve C., Bachmann O., Burgisser

A., Characterization of juvenile pyroclasts from the Kos Plateau Tuff (Aegean Arc): insights into the eruptive dynamics of a large rhyolitic eruption, Bulletin of Volcanology DOI 10.1007/s00445-008-0250-x, 2008

[41] Degruyter W., Bachmann O., Burgisser A., Controls on magma outgassing in the volcanic conduit during the climactic phase of the Kos Plateau Tuff eruption (Aegean Arc), Bulletin of Volcanology 72, 2009, 63-74

[42] Best M.G., Christiansen E.H., Origin of broken crystals in ash-flow tuffs, Geological Society of America Bulletin 109, 1997, 63-73

[43] Bouvet de Maisonneuve C., Bachmann O., Burgisser A., Characterization of juvenile pyroclasts from the Kos Plateau Tuff (Aegean Arc): insights into the eruptive dynamics of a large rhyolitic eruption, Bulletin of Volcanology 71, 2009, 643-658

[44] Burt R.M., Brown S.J.A., Cole J.W., Shelley D., Waight T.E., Glass-bearing plutonic fragments from ignimbrites of the Okataina caldera complex, Taupo Volcanic Zone, New Zealand: remnants of a partially molten intrusion associated with preceding eruptions, Journal of Volcanology and Geothermal Research 84, 1998, 209-237

[45] Brown S.J.A., Burt R.M., Cole J.W., Krippner S.J.P., Price R.C., Cartwright I., Plutonic lithics in ignimbrites of the Taupo Volcanic Zone, New Zealand; sources and conditions of crystallization, Journal of Volcanology and Geothermal Research 148, 1998, 21-41

[46] Charlier B.L.A., Peate D.W., Wilson C.J.N., Lowenstern J.B., Storey M., Brown S.J.A., Crystallisation ages in coeval silicic magma bodies: 238U-230Th disequilibrium evidence from the Rotoiti and Earthquake Flat eruption deposits, Taupo Volcanic Zone, New Zealand, Earth and Planetary Science Letters 206, 2003, 441-457

[47] Pe-Piper G., Moulton B., Magma evolution in the Pliocene-Pleistocene succession of Kos, South Aegean arc (Greece), Lithos 106, 2008, 110-124

[48] Briqueu L., Javoy M., Lancelot J.R., Tatsumoto M., Isotope geochemistry of recent magmatism in the Aegean arc: Sr, Nd, Hf, and O isotopic ratios in the lavas of Milos and Santorini - geodynamic implications, Earth and Planetary Science Letters 80, 1986, 41-54

[49] Druitt T.H., Edwards L., Mellors R.M., Pyle D.M., Sparks R.S.J., Lanphere M., Davies M., Barriero B., Santorini Volcano, Geological Society Memoir, London, 1999

[50] Pe-Piper G., Hatzipanagiotou K., The Pliocene volcanic rocks of Crommyonia, western Greece and their implications for the early evolution of the South Aegean arc, Geological Magazine 134, 2000, 55-66

[51] Weldeab S., Emeis K.-C., Hemleben C., Siebel W., Provenance of lithogenic surface sediments and pathways of riverine suspended matter in the Eastern Mediterranean Sea: evidence from 143Nd/144Nd and 87Sr/86Sr ratios, Chemical Geology 186, 2002, 139-149

[52] Krom M.D., Cliff R.A., Eijsink L.M., Herut B., Chester R., The characterisation of Saharan dusts and Nile particulate matter in surfacesediments from the Levantine basin using Sr isotopes, Marine Geology 155, 1999, 319-330

[53] Bachmann O., Bergantz G.W., Rhyolites and their Source Mushes across Tectonic Settings, Journal of Petrology 49, 2008, 2277-2285

[54] Bachmann O., Wallace P.J., Bourquin J., The melt inclusion record from the rhyolitic Kos Plateau Tuff (Aegean Arc), Contributions to Mineralogy and Petrology, DOI 10.1007/s00410-009-0423-4, 2009

[55] Housh T.B., Luhr J.F., Plagioclase-melt equilibria in hydrous systems, American Mineralogist 76, 1991, 477-492

[56] Blundy J., Cashman K., Ascent-driven crystallisation of dacite magmas at Mount St Helens, 1980-1986, Contributions to Mineralogy and Petrology 140, 2001, 631-650

[57] Sederholm J.J., Uder die finnländischen Rapakivigesteine, Tschermak's Mineralogische und Petrographische Mitteilungen 12, 1891, 1-31

[58] Wark D.A., Stimac J.A., Origin and mantled (rapakivi) feldspars; experimental evidence of a dissolution- and diffusion-controlled mechanism, Contributions to Mineralogy and Petrology 111, 1992, 345-361

[59] Stimac J.A., Wark D.A., Plagioclase mantles on sanidine in silicic lavas, Clear Lake, California; implications for the origin of rapakivi texture, Geological Society of America Bulletin 104, 1992, 728-744

[60] Bachmann O., Dungan M.A., Lipman P.W., The Fish Canyon magma body, San Juan volcanic field, Colorado: rejuvenation and eruption of an upper crustal batholith, Journal of Petrology 43, 2002, 1469-1503

[61] C. Zhu, H. Xu, E.S. Ilton, D.R. Veblen, D.J. Henry, M.K. Tivey, G. Thompson, TEM-AEM observations of Cl-rich amphibole and biotite and possible petrologic implications, American MIneralogist 79, 1994, 909-920

[62] Deer W.A., Howie R.A., Zussman J., An introduction to the rock-forming minerals, Longman Group Ltd, 1992

[63] Harris A.C., Kamenetsky V.S., White N.C., Van

Achterbergh E., Ryan C.G., Melt Inclusions in Veins: Linking Magmas and Porphyry Cu deposits, Science 302, 2003, 2109-2111

[64] Hildreth W., The magma chamber of the BishopTuff: gradients in temperature, pressure, and composition, Ph.D thesis, University of California, Berkeley, 1977

[65] Munoz J.L., F-OH and Cl-OH exchange in micas with applications to hydrothermal ore deposits., Bailey, S.W. (Ed.), Reviews in Mineralogy, Mineralogical Society of America 13, 1984, 469-493

[66] Bacon R.C., Hirschmann M.M., Mg/Mn partitioning as a test for equilibrium between coexisting Fe-Ti oxides, American Mineralogist 73, 1988, 57-61

[67] Bindeman I.N., Fragmentation phenomena in populations of magmatic crystals, American MIneralogist 90, 2005, 1801-1815

[68] Wark D.A., Spear F.S., Titanium in quartz: Cathodoluminescence and thermometry, Geochimica et Cosmochimica Acta Suppl. 69, 2005, A592

[69] Wark D., Watson E., TitaniQ: a titanium-in-quartz geothermometer, Contributions to Mineralogy and Petrology 152, 2006, 743-754

[70] Peppard B.T., Steele I.M., Davis A.M., Wallace P.J., Anderson A.T., Zoned quartz phenocrysts from the rhyolitic Bishop Tuff, American Mineralogist 86, 2001, 1034-1052

[71] Esawi E.K., AMPH-CLASS: An Excel spreadsheet for the classification and nomenclature of amphiboles based on the 1997 recommendations of the International Mineralogical Association, Computers & Geosciences 30, 2004, 753-760

[72] Ghiorso M.S., Evans B.W., Thermodynamics of rhombohedral oxide solid solutions and a revision of the Fe-Ti oxide geothermometer and oxygen-barometer, American Journal of science 308, 2008, 957-1039

[73] Andersen D.J., Lindsley D.H., New (and final!) models for the Ti-magnetite/ ilmenite geothermometer and oxygen barometer, in: T. Eos, American Geophysical Union, (Ed.), AGU Spring meeting 66, American Geophysical Union. Washington, DC, Baltimore, MD, 1985

[74] Scaillet B., Evans B.W., The 15 June 1991 eruption of Mount Pinatubo. I. Phase equilibria and pre-eruption P-$T - fO_2 - fH_2O$ conditions of the dacite magma, Journal of Petrology 40, 1999, 381-411

[75] Wallace P., From mantle to atmosphere: Magma degassing, explosive eruptions, and volcanic volatile budgets, in: B. De Vivo, R.J. Bodnar, (Eds.), Melt Inclusions in Volcanic Systems: Methods, Applications and Problems 5, Elsevier Science, Developments in Volcanology, 2003, 105-127

[76] Streck M.J., Dilles J.H., Sulfur evolution of oxidized arc magmas as recorded in apatite from a porphyry copper batholith, Geology 26, 1998, 523-526

[77] Bernard A., Demaiffe D., Mattielli N., Punongbayan R.S., Anhydrite-bearing pumices from Mount Pinatubo: further evidence for the existence of sulphur-rich silicic magmas, Nature 354, 1991, 139-140

[78] Parat F., Dungan M.A., Streck M.J., Anhydrite, pyrrhotite, and sulfur-rich apatite: tracing the sulfur evolution of an Oligocene andesite (Eagle Mountain, CO, USA), Lithos 64, 2002, 63-75

[79] Wen S., Nekvasil H., SOLVCALC; an interactive graphics program package for calculating the ternary feldspar solvus and for two-feldspar geothermometry, Computers and Geosciences 20, 1994, 1025-1040

[80] Holland T., Blundy J., Non-ideal interactions in calcic amphiboles and their bearing on amphibole-plagioclase thermometry, Contributions to Mineralogy and Petrology 116, 1994, 433-447

[81] Chiba H., Chacko T., Clayton R.N., Goldsmith J.R., Oxygen isotope fractionations involving diopside, forsterite, magnetite, anc calcite: application to geothermometry, Geochimica and Cosmochimica Acta 53, 1989, 2985-2995

[82] Watson E.B., Harrison T.M., Zircon saturation revisited: temperature and composition effects in a variety of crustal magma types, Earth and Planetary Science Letters 64, 1983, 295-304

[83] Lepage L.D., ILMAT: An Excel worksheet for ilmenite-magnetite geothermometry and geobarometry, Computers & Geosciences 29, 2003, 673-678

[84] Johannes W., Holtz F., Petrogenesis and experimental petrology of granitic rocks, Springer-Verlag, 1996

[85] Hayden L.A., Watson E.B., Rutile saturation in hydrous siliceous melts and its bearing on Ti-thermometry of quartz and zircon, Earth and Planetary Science Letters 258, 2007, 561-568

[86] Mitropolous P., Tarney J., Saunders A.D., Marsh N.G., Petrogenesis of cenozoic rocks from the aegean island arc, Journal of Volcanology and Geothermal Research 32, 1987, 177-193

[87] Altherr R., Henjes-Kunst F., Matthews F., Friedrichsen H., Hansen B.T., O-Sr isotopic variations in Miocene granitoids from the Aegean: evidence for an origin by combined assimilation and fractional crystallization, Contributions to Mineralogy and Petrology 100, 1988, 528-541

[88] Pe-Piper G., Piper D.J.W., Late Cenozoic, post-collisional Aegean igneous rocks: Nd, Pb, and Sr isotopic constraints on petrogenetic and tectonic models, Geological Magazine 138, 2001, 653-668

[89] Pe-Piper G., Piper D.J.W., The igneous rocks of

Greece, Gebrüder Borntreager, Berlin, 2002, 573 pp.
[90] Witt-Eickschen G., Seck H.A., Mezger K., Eggins S.M., Altherr R., Lithospheric Mantle Evolution beneath the Eifel (Germany): Constraints from Sr-Nd-Pb Isotopes and Trace Element Abundances in Spinel Peridotite and Pyroxenite Xenoliths, J. Petrology 44, 2003, 1077-1095
[91] Hawkesworth C.J., Vollmer R., Crustal contamination versus enriched mantle: 143Nd/144Nd and 87Sr/86Sr evidence from the Italian volcanics, Contributions to Mineralogy and Petrology 69, 1979, 151-165
[92] Pe-Piper G., Piper D.J.W., Upper-Miocene Igneous Rocks of Samos: The Role of Tectonism in Petrogenesis in the Southeastern Aegean, Geological Society of London, Special Publication 291, 2007, 75-97
[93] Robert U., Foden J., Varne R., The Dodecanese Province, SE Aegean: A model for tectonic control on potassic magmatism, Lithos 28, 1992, 241-260
[94] Mitropoulos P., Tarney J., Saunders A.D., Marsh N.G., Petrogenesis of cenozoic rocks from the aegean island arc, Journal of Volcanology and Geothermal Research 32, 1987, 177-193
[95] Eiler J.M., Schiano P., Kitchen N., Stolper E.M., Oxygen-isotope evidence for recycled crust in the sources of mid-ocean-ridge basalts, Nature 403, 2000, 530-534
[96] Bindeman I.N., Oxygen isotopes in mantle and crustal magmas as revealed by single crystal analysis, in: Putirka K.D., Tepley F.J., (Eds.), Minerals, inclusions and volcanic processes 69, Reviews in Mineralogy and Geochemistry vol 69, 2008, 445-478
[97] Ducea M.N., Barton M.D., Igniting flare-up events in Cordilleran arcs, Geology 35, 2007, 1047-1050
[98] Taylor H.P., The effects of assimilation of country rocks by magmas on $^{18}O/^{16}O$ and $^{87}Sr/^{86}Sr$ systematics in igneous rocks, Earth and Planetary Science Letters 47, 1980, 243-254
[99] Pearson D.G., Davies G.R., Nixon P.H., Greenwood P.B., Mattey D.P., Oxygen isotope evidence for the origin of pyroxenites in the Beni Bousera peridotite massif, North Marocco: derivation from subducted oceanic lithosphere, Earth and Planetary Science Letters 102, 1991, 289-301
[100] Harmon R.S., Hoefs J., Oxygen isotope heterogeneity of the mantle deduced from global O18 systematics of basalts from different geotectonic settings, Contributions to Mineralogy and Petrology 120, 1995, 95-114
[101] de Celles P.G., Ducea M.N., Kapp P., Zandt G., Cyclicity in Cordilleran orogenic systems, Nature Geoscience 2, 2009, 251-257
[102] Dufek J., Bergantz G.W., Lower Crustal Magma Genesis and Preservation: a Stochastic Framework for the Evaluation of Basalt-Crust Interaction, Journal of Petrology 46, 2005, 2167-2195
[103] Annen C., Blundy J.D., Sparks R.S.J., The genesis of calc-alkaline intermediate and silicic magmas in deep crustal hot zones, Journal of Petrology 47, 2006, 505-539
[104] Bunsen R., Ueber die prozesse der vulkanishen Gesteinsbildungen Islands, Annalen der Physics (Leipzig) 83, 1851, 197-272
[105] Larsen E.S., Irving J., Gonyer F.A., Larsen E.S.R., Petrologic results of a study of the minerals from the tertiary volcanic rocks of the San Juan region, Colorado, American MIneralogist 21, 22, 23, 1938
[106] Dufek J., Bachmann O., Quantum magmatism, Geology(in press).
[107] White S.M., Crisp J.A., Spera F.A., Long-term volumetric eruption rates and magma budgets, Geochem. Geophys. Geosyst. 7, 2006
[108] Piper D., Pe-Piper G., Lefort D., Precursory activity of the 161 ka Kos Plateau Tuff eruption, Aegean Sea (Greece), Bulletin of Volcanology
[109] Bachmann O., Bergantz G.W., Gas percolation in upper-crustal silicic crystal mushes as a mechanism for upward heat advection and rejuvenation of near-solidus magma bodies, Journal of Volcanology and Geothermal Research 149, 2006, 85-102
[110] Bachmann O., Bergantz G.W., Rejuvenation of the Fish Canyon magma body: a window into the evolution of large-volume silicic magma systems, Geology 31, 2003, 789-792
[111] Kent A.J.R., Blundy J., Cashman K.V., Cooper K.M., Donnelly C., Pallister J.S., Reagan M., Rowe M.C., Thornber C.R., Vapor transfer prior to the October 2004 eruption of Mount St. Helens, Washington, Geology 35, 2007, 231-234
[112] Boyce J.W., Hervig R.L., Magmatic degassing histories from apatite volatile stratigraphy, Geology 36, 2008, 63-66
[113] Shimizu A., Sumino H., Nagao K., Notsu K., Mitropoulos P., Variation in noble gas isotopic composition of gas samples from the Aegean arc, Greece, Journal of Volcanology and Geothermal Research 140, 2005, 321-339
[114] Annen C., Blundy J., Sparks R.S.J., The sources of granitic melt in Deep Hot Zones, Transactions of the Royal Society of Edimburgh: Earth Sciences 97, 2007
[115] Lagios E., Sakkas V., Parcharidis I., Dietrich V., Ground deformation of Nisyros Volcano (Greece)

for the period 1995-2002: Results from DInSAR and DGPS observations, Bulletin of Volcanology 68, 2005, 201-214

[116] Papadopoulos, Sachpazi, Panopoulou, Stavrakakis, The volcanoseismic crisis of 1996-97 in Nisyros, SE Aegean Sea, Greece, Terra Nova 10, 1998, 151-154

[117] Mitropolous P., Tarney J., Stouraiti C., Notsu K., Arakawa Y., Sr isotoppic vation along the Aegean Arc: Constraints on magma genesis on the basis of new Sr isotopic data, Bulletin of the Geological Society of Greece 32, 1998, 225-230

[118] Altherr R., Siebel W., I-type plutonism in a continental back-arc setting: Miocene granitoids and monzonites from the central Aegean Sea, Greece, Contributions to Mineralogy and Petrology 143, 2002, 397-415

[119] Whitney J.A., Stormer J.C., Igneous sulfides in the Fish Canyon Tuff and the role of sulfur in calc-alkaline magmas, Geology 11, 1983, 99-102

[120] Bindeman I.N., Valley J.W., Oxygen isotope study of the Long Valley magma system, California: isotope thermometry and convection in large silicic magma bodies, Contributions to Mineralogy and Petrology 144, 2002, 185-205